Frontiers in Physics

TYPE Original Research
PUBLISHED 12 January 2026
DOI 10.3389/fphy.2026.1717438

Broad bandgap tuning and emission interplay between silicon quantum dots and defect states in RF-sputtered silicon oxynitride thin films

Luis Fernando Garrido-García[1], Ana Laura Pérez-Martínez[2], Alejandra López-Suárez[1], María del Pilar Aguilar-Del-Valle[2] and Arturo Rodríguez-Gómez[1]*

[1]Instituto de Física, Universidad Nacional Autónoma de México, Circuito de la Investigación Científica s/n, Ciudad Universitaria, Ciudad de México, Mexico, [2]Facultad de Ingeniería, División de Ciencias Básicas, Universidad Nacional Autónoma de México, Circuito exterior s/n, Ciudad Universitaria, Ciudad de México, Mexico

Silicon oxynitride (SiON) thin films were grown by RF magnetron sputtering system (RF-MS) from both pure and silicon-enriched Si_3N_4 targets, enabling systematic exploration of substrate temperature, RF power, and target composition. The resulting materials diverge from conventional stoichiometric SiON, forming silicon-rich, non-stoichiometric films whose optical and structural responses are strongly parameter-dependent. The effective optical bandgap was tuned across 2.17–3.09 eV, driven by the interplay of oxygen incorporation, defect states, and the emergence of embedded Si nanoclusters. The refractive index spanned 1.41–2.11, mapping a broad compositional continuum across the studied deposition conditions. Microstructural analyses by SEM, TEM, and diffraction revealed that silicon inserts promote localized crystallinity and the formation of quantum-dot-like domains. These features correlate with a sharp photoluminescence peak at 3.24 eV. Surface characterization by AFM showed that roughness is critically governed by RF power and temperature, with silicon inserts further amplifying nanoscale disorder. Film thickness scaled with power and time, exceeding 2 µm under high-power, high-temperature, insert-modified conditions. Together, these results demonstrate that careful tuning of sputtering parameters provides access to non-stoichiometric SiON thin films with controllable bandgap, refractive index, and microstructure, making them particularly promising for planar optical waveguide integration, near-UV/blue light-emitting layers, and (complementary metal–oxide–semiconductor) CMOS-compatible photonic and sensing platforms.

KEYWORDS

broad bandgap engineering (2.17–309 eV) in SiON, near-UV/blue photoluminescence (3.24 eV emission), non-stoichiometric silicon oxynitride (SiOxNy) thin films, RF magnetron sputtering, silicon oxynitride thin films, silicon quantum dots, silicon quantum dots/Si nanoclusters in SiON

OPEN ACCESS

EDITED BY
Engin Deligoz,
Aksaray University, Türkiye

REVIEWED BY
Harshita Rai,
Kyushu Institute of Technology, Japan
Tri Nguyen,
Stanford University, United States

*CORRESPONDENCE
Arturo Rodríguez-Gómez,
arodriguez@fisica.unam.mx

RECEIVED 02 October 2025
REVISED 28 December 2025
ACCEPTED 02 January 2026
PUBLISHED 12 January 2026

CITATION
Garrido-García LF, Pérez-Martínez AL, López-Suárez A, Aguilar-Del-Valle MdP and Rodríguez-Gómez A (2026) Broad bandgap tuning and emission interplay between silicon quantum dots and defect states in RF-sputtered silicon oxynitride thin films. *Front. Phys.* 14:1717438. doi: 10.3389/fphy.2026.1717438

1 Introduction

Silicon oxynitride (SiON) is a compound that results from combining stoichiometric silicon nitride (Si_3N_4) and silicon dioxide (SiO_2) in different proportions [1]. Owing to its mixed nature, SiON is a highly tunable material with attractive physical and optical properties. This versatility has enabled its use in diverse applications such as diffusion barriers and passivation layers in CMOS devices [2–5], transparent non-volatile memories [6], integrated photonic circuits [7, 8], electroluminescent devices [9], optical waveguides [10, 11], and scratch-resistant coatings [12].

A particularly relevant example is its role in planar optical waveguides, where SiON films serve as guiding layers with refractive indices tunable between 1.45 (SiO_2) and 2.0 (Si_3N_4), enabling flexible index contrast design and low propagation losses (~0.2 dB/cm) [7, 10, 13, 14]. In coatings, the composition-dependent hardness of SiON (7.4–16.2 GPa) has been exploited to fabricate scratch-resistant antireflective (SRAR) films combining mechanical durability with low reflectance (<1%) [12]. Beyond photonics and protective layers, SiON has also been investigated as a flexible barrier for organic solar cells [5], as a passivation layer in thin-film transistors [4], and in nonlinear optics due to its large and tunable optical bandgap and strong second-harmonic generation (SHG) [2, 8, 15–17].

Given these wide-ranging applications, significant effort has been devoted to optimizing SiON thin-film growth by chemical vapor deposition (CVD) [18, 19], plasma-enhanced CVD (PECVD) [20, 21], and remote PECVD (RPECVD) [22–27]. While effective, these techniques rely on hazardous precursor gases, require substrate temperatures above 400 °C, and typically yield films with unwanted hydrogen incorporation [8, 28]. In contrast, sputtering offers a safer and more environmentally friendly alternative, eliminating toxic precursors, reducing chemical waste, and enabling deposition at lower thermal budgets [29, 30]. Beyond its economic and environmental benefits, sputtering is consistent with several United Nations Sustainable Development Goals (SDGs), such as SDG 3 (Good Health and Wellbeing), SDG 7 (Affordable and Clean Energy), and SDG 13 (Climate Action) [31, 32].

Several studies have investigated the effects of chamber pressure [33], substrate temperature [34], working gas flow [35, 36], and RF power [37, 38] on the properties of sputtered SiON films. For instance, De Luca et al. demonstrated refractive-index tuning in the 1.5–2.5 range by modulating RF power during reactive sputtering [38], while earlier work by Mirsch and Bauer showed that both refractive index and optical bandgap can be adjusted through control of oxygen partial pressure and substrate temperature [34]. In contrast, Dergez et al. investigated silicon-rich nitride films deposited from a pure Si target, reporting refractive-index values largely independent of deposition conditions [33]. Collectively, these studies establish RF sputtering as a versatile technique for tuning SiON optical constants; however, they rely on conventional target compositions and gas-phase control, which intrinsically limit the accessible compositional and electronic regimes.

In this context, enriching a Si_3N_4 target with crystalline silicon inserts defines a distinct and previously unexplored parameter space in RF sputtering. Unlike conventional reactive sputtering approaches, where film composition is primarily controlled through gas-phase ratios or plasma conditions, the insert-based strategy introduces a localized and controllable excess of elemental Si directly at the target. This enables access to strongly silicon-rich, non-stoichiometric SiON compositions that are not readily achievable through standard routes.

In this work, we investigate the combined influence of RF power, substrate temperature, and the enrichment of Si_3N_4 targets with pure silicon inserts on the optical and microstructural properties of SiON thin films deposited by RF-MS. This approach provides a route to silicon-rich, non-stoichiometric SiON films whose properties deviate significantly from those of conventional stoichiometric SiON. In particular, our study demonstrates that the effective optical bandgap enables effective bandgap tuning over the 2.17–3.09 eV range, substantially lower than the 5–9 eV typically reported for stoichiometric SiON [39], due to the combined effects of non-stoichiometry, defect-related states, and the formation of Si nanoclusters. Furthermore, we show that target enrichment promotes localized crystallinity and quantum-dot-like nanostructures, while substrate temperature and sputtering power critically govern roughness and morphology. These insights highlight the potential of sputtering-based strategies to engineer non-stoichiometric SiON thin films with tailored optical and structural characteristics for optoelectronic and photonic applications.

2 Methodology

Thin films of SiON were deposited on high-resistivity silicon wafers, glass, copper grids for TEM, and fused silica plates. Films on silicon wafers were used for FTIR, SEM, and ellipsometry; fused silica substrates for UV-Vis spectroscopy; and TEM grids for high-resolution transmission electron microscopy (HRTEM). Substrates were carefully cut and cleaned to remove surface contaminants. Glass slides (1 × 2.5 cm) were cut with a diamond-tip pen, silicon wafers were immersed in methanol for 5 min, and quartz and glass samples underwent sequential ultrasonic baths in trichloroethylene, methanol, acetone, and methanol (5 min each) [40]. For TEM, copper grids were precoated with a thin collodion layer to provide mechanical support; in cases of high-temperature depositions, films were scraped onto these grids for imaging. A CO_2 jet gun (model K1-10, CO_2Clean) was used at the final stage to remove residual dust and prevent drying stains.

To enrich the silicon content, six crystalline silicon discs (3 mm in diameter) were embedded into the erosion track of the Si_3N_4 target. Cavities were cut with a GATAN model 601 ultrasonic cutter to secure the inserts and enlarge adhesion regions, thereby minimizing adhesive-plasma interaction and avoiding cyanoacrylate contamination. The resulting modified target is shown in Figure 1.

Depositions were performed using the RF-MS system developed by the Silicon Photonics Research Group at IFUNAM, whose configuration is illustrated in Figure 2. The system consists of a 4 L spherical ISO-100 reaction chamber evacuated by a two-stage direct-drive mechanical pump (190 L/min) and an Agilent V-81 turbomolecular pump (67 L/s at 81,000 rpm) controlled by a TwisTorr 304FS unit. A 1-inch planar NdFeB magnetron was used for RF sputtering.

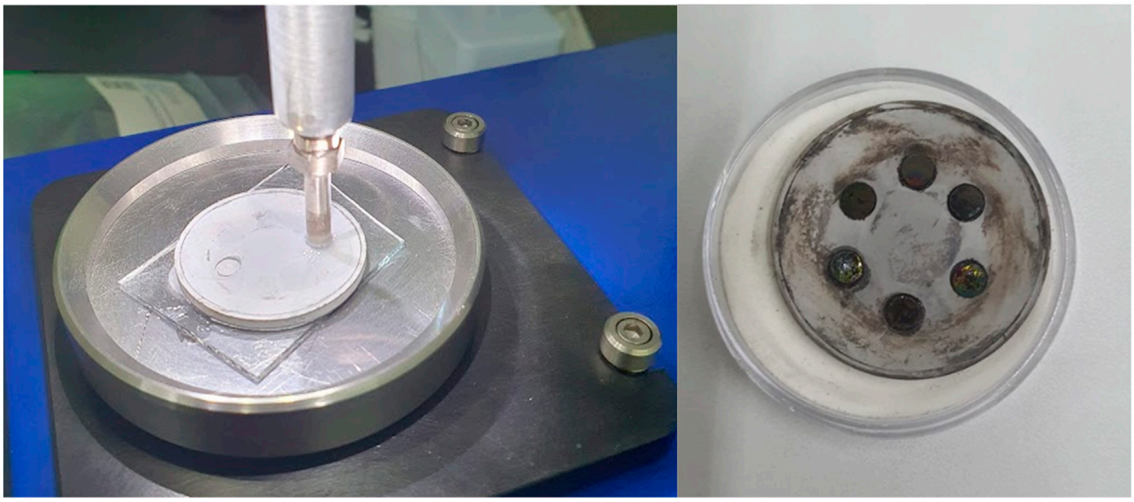

FIGURE 1
Modification of the Si_3N_4 sputtering target with six crystalline silicon discs (3 mm diameter) embedded in the toroidal erosion zone. This configuration was used to enrich the sputtered films with additional silicon and minimize plasma-adhesive interaction during RF deposition.

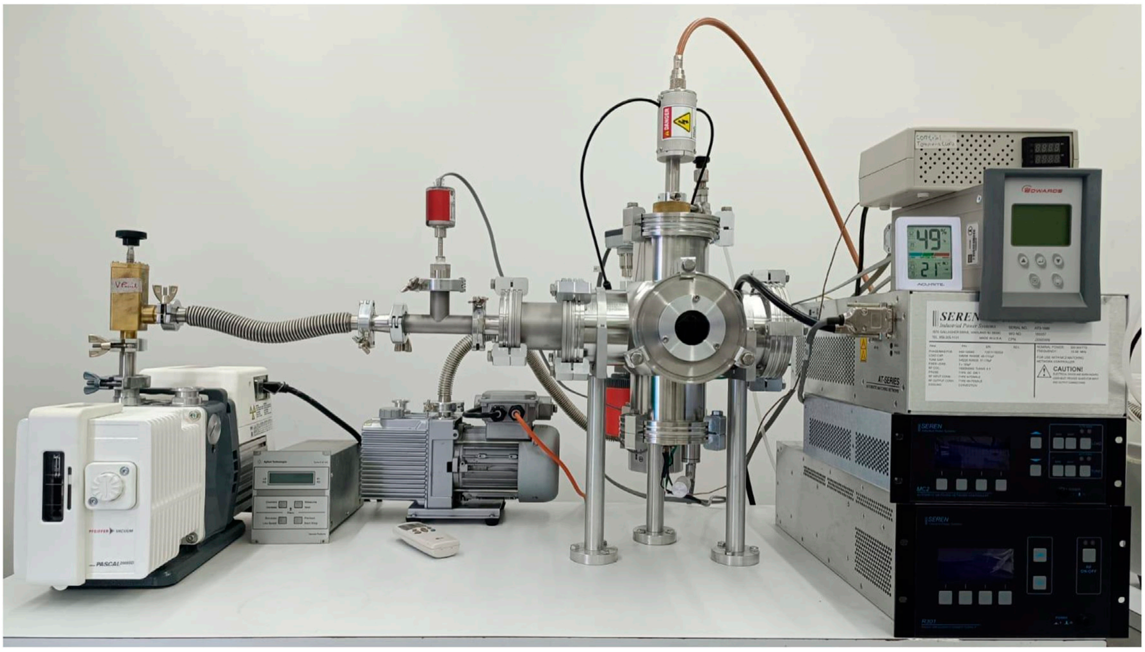

FIGURE 2
Custom-built RF magnetron sputtering system (Mini-Sputtering) developed by the Silicon Photonics Research Group at IFUNAM. The setup includes a spherical reaction chamber, mechanical and turbomolecular pumping, and a 1-inch RF magnetron.

RF excitation was supplied by a 13.56 MHz SEREN R301 RF source coupled to an AT3 automatic matching network and an MC2 controller. Base pressure was maintained at ~2.0×10^{-5} Torr, with an argon working pressure of 40 mTorr and a target-substrate distance of 5 cm.

Deposition parameters including RF power (25, 50, and 75 W), time (10–120 min), and substrate temperature (room temperature (RT) or 300 °C) were systematically varied, with and without silicon inserts. The nomenclature and conditions for each deposition are summarized in Table 1.

Because oxygen incorporation plays a critical role in the formation of SiON, the stability of the pre-deposition vacuum was verified before each run. Although the system reached a base pressure of ~2×10^{-5} Torr, the residual O_2/H_2O content was not directly monitored with a residual gas analyzer (RGA). At this vacuum level, the background is typically dominated by water and

TABLE 1 Experimental conditions matrix for the deposition of SiON thin films by RF-MS. Samples were grown from pure Si_3N_4 targets and from targets enriched with Si inserts, at room temperature (RT) or 300 °C. The nomenclature indicates the applied RF power (25–75 W), deposition time (10–120 min), substrate temperature (RT or 300 °C), and target composition (pure or with Si inserts). For example, "75W60mRT pure" corresponds to a film deposited at 75 W for 60 min at room temperature using a pure Si_3N_4 target, while "25W60m300 inserts" indicates a film deposited at 25 W for 60 min at 300 °C from a target with Si inserts.

SiON target room temperature	SiON target w/inserts room temp	SiON target 300 °C	SiON target w/inserts 300 °C
75W10mRT pure	25W60mRT inserts	25W120m300 pure	25W60m300 inserts
75W30mRT pure	25W90mRT inserts	25W60m300 pure	25W120m300 inserts
75W60mRT pure	25W120mRT inserts	25W90m300 pure	25W90m300 inserts
50W30mRT pure	50W60mRT inserts	75W10m300 pure	50W60m300 inserts
50W60mRT pure	50W30mRT inserts	75W60m300 pure	50W30m300 inserts
25W60mRT pure	75W60mRT inserts	50W60m300 pure	75W60m300 inserts
25W90mRT pure	75W30mRT inserts	75W30m300 pure	75W30m300 inserts

oxygen desorbed from chamber walls, which is a well-known source of oxygen incorporation in non-reactive sputtering. Therefore, the oxygen detected in the films is reasonably attributed to residual background species (O_2 and H_2O) released from chamber surfaces, a process that occurs at all deposition temperatures and is enhanced by thermally activated desorption during depositions performed at 300 °C.

Although the residual gas composition was not directly measured, the base pressure and deposition parameters were kept constant for all runs, resulting in reproducible oxygen incorporation levels across samples deposited under identical conditions.

Film morphology was analyzed using a JEOL JSM-7800F SEM at the Central Microscopy Laboratory (LCM), IFUNAM. To minimize beam damage, accelerating voltages as low as 1 kV were used, with working distances of 3.5 mm and probe current of 9. Images were recorded at magnifications between 10k × and 200k × using JEOL PC SEM software. Structural characterization was complemented with a JEOL JEM-2010 FEG TEM (200 kV, 0.5 mm Cs, 0.19 nm resolution, 1 M × magnification), from which bright-field, HRTEM, and diffraction images were obtained to assess crystallinity and nanostructural features.

3 Results and discussion

3.1 Plasma spectroscopy

Optical emission spectroscopy (OES) was performed using an Ocean Optics Flame spectrometer to monitor plasma species during sputtering. Twenty spectra were recorded at equal time intervals throughout deposition and averaged over the 680–860 nm range with 0.38 nm resolution. The highest emission intensities were consistently observed under room-temperature conditions, regardless of whether the target was pure or modified with Si inserts, Figure 3. This suggests that substrate heating to 300 °C increases energy transfer to the target, enhancing sputtering yield and consequently lowering the concentration of free argon atoms available for excitation and emission [41].

The spectra were highly reproducible, with negligible peak shifts and only minor intensity variations. All peaks were assigned to argon transitions based on the NIST database [42], with no detectable emission from target species (Si, N, O). The strong argon lines in the red, orange, and violet regions are consistent with the characteristic pink-purple plasma glow. This confirms that the discharge is argon-dominated and stable across all conditions. Such stability ensures that the observed changes in film composition, microstructure, and optical properties originate from surface growth dynamics rather than fluctuations in plasma chemistry, validating OES as a supporting diagnostic for process reproducibility.

3.2 Scanning electron microscopy (SEM)

The surface morphology of the SiON thin films was examined by SEM at 50k magnifications to assess uniformity, compactness, and nanoscale texture as a function of RF power, substrate temperature, and target composition (pure Si_3N_4 vs. Si-insert-enriched). These attributes are directly relevant to optical performance, as surface disorder increases scattering and biases refractive index/absorption retrieval; quantitative roughness metrics are reported by AFM in Section 3.4.

At 25 W, the films obtained from the pure target display a continuous and featureless surface, indicative of dense coverage. In contrast, those grown with Si inserts already show protrusions and local defects at room temperature, evidencing early-stage three-dimensional nucleation. Heating to 300 °C improves compaction for the pure target, whereas for insert-containing samples it enhances the size and definition of surface features, consistent with Si-rich clustering. These results are shown in Figure 4.

At 50 W, all films become more uniformly textured. The pure-target series at both room temperature and 300 °C exhibits the smoothest appearance across the dataset, suggesting an

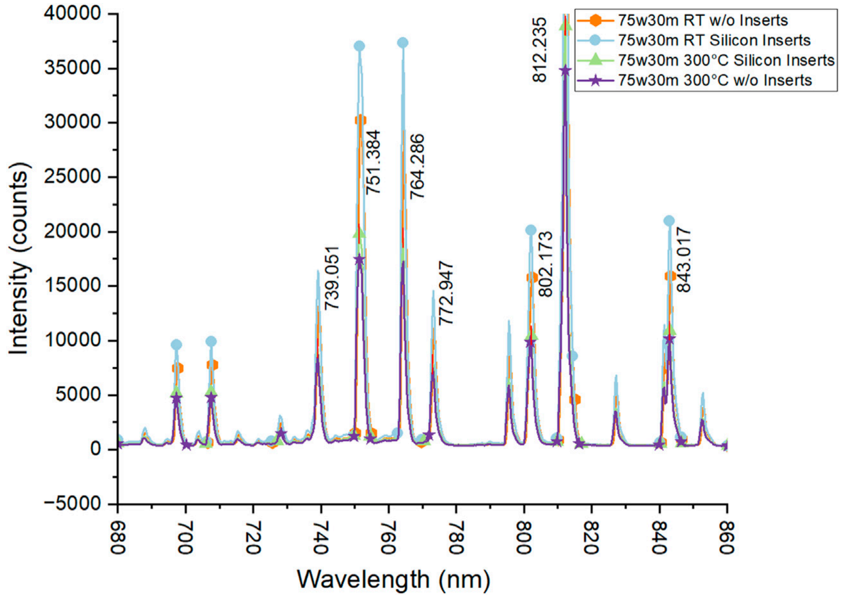

FIGURE 3
Spectroscopy of sputtering plasma at 75 W for 30 min and variations in substrate temperature and target homogeneity.

optimal balance between arrival flux and adatom mobility. Insert-containing films remain granular but more homogeneous than those grown at 25 W, pointing to improved coalescence. Representative morphologies are presented in Figure 5.

At 75 W, the pure-target series still produces dense granular surfaces. However, when Si inserts are combined with heating at 300 °C, faceted, flake-like aggregates emerge, with pronounced roughening. This behavior indicates a transition toward three-dimensional growth when a high Si-rich flux coincides with elevated adatom mobility, favoring clustering and partial phase separation. The corresponding SEM images are provided in Figure 6.

Overall, SEM indicates that (i) Si inserts systematically drive the surface toward granular and three-dimensional morphologies, particularly at elevated temperature; (ii) 50 W provides the smoothest, most homogeneous surfaces across conditions; and (iii) the 75 W + inserts +300 °C combination maximizes surface disorder. These qualitative trends align with AFM roughness measurements (Section 3.4) and with the observed optical behavior, namely reduced transmittance for insert-containing films at high temperature, supporting a growth picture where target enrichment and thermal budget jointly modulate surface diffusion and Si nanocluster formation.

3.2.1 Thickness measurement of silicon oxynitride films by SEM cross-section

The thickness of the SiON thin films was evaluated from cross-sectional SEM images, as illustrated in Figure 7. The average values obtained for each deposition condition are summarized in Table 2. Film thickness exhibited a strong dependence on the sputtering parameters, particularly RF power, deposition time, substrate temperature, and the incorporation of silicon inserts into the target.

To determine the average film thickness, cross-sectional SEM images were analyzed by taking measurements at regular intervals along the thickness of each layer, with each reported value representing the average of ten point measurements. Because the raw SEM measurements inherently show small numerical fluctuations at the nanometer scale, the averaged values were subsequently rounded to one decimal place to ensure consistency and to reflect the practical precision of the SEM technique. This level of rounding is appropriate because the intrinsic measurement uncertainty of SEM cross-sectional thickness analysis is larger than the third decimal place. Therefore, values such as 2000 nm correspond to rounded averages derived from the underlying set of ten measurements.

A general trend was observed in which thickness increased with both RF power and deposition time, reflecting the higher sputtering yield and enhanced deposition rate at elevated energies. Substrate heating to 300 °C further promoted film growth, which can be attributed to the increased surface mobility of adatoms and a reduction of re-sputtering effects, leading to more compact and thicker films.

The inclusion of silicon inserts also had a marked impact. In several conditions, particularly at intermediate and high powers, the inserts promoted the formation of thicker layers, suggesting that target enrichment with Si modifies the sputtering dynamics. This effect may arise from the higher sputtering yield of silicon relative to silicon nitride, combined with changes in secondary electron emission and plasma-target coupling efficiency, ultimately enhancing local erosion of the Si inserts and altering the plasma chemistry that governs film growth. However, in some low-power conditions, the inserts did not enhance thickness significantly, pointing to a threshold dependence on discharge energy.

Resputtering contributes to the observed nonlinearity in growth, particularly at higher RF powers. More energetic ions and neutrals can re-etch the growing film, partially removing previously deposited material and reducing the net deposition rate. This effect intensifies as power increases, modifying both the vertical growth

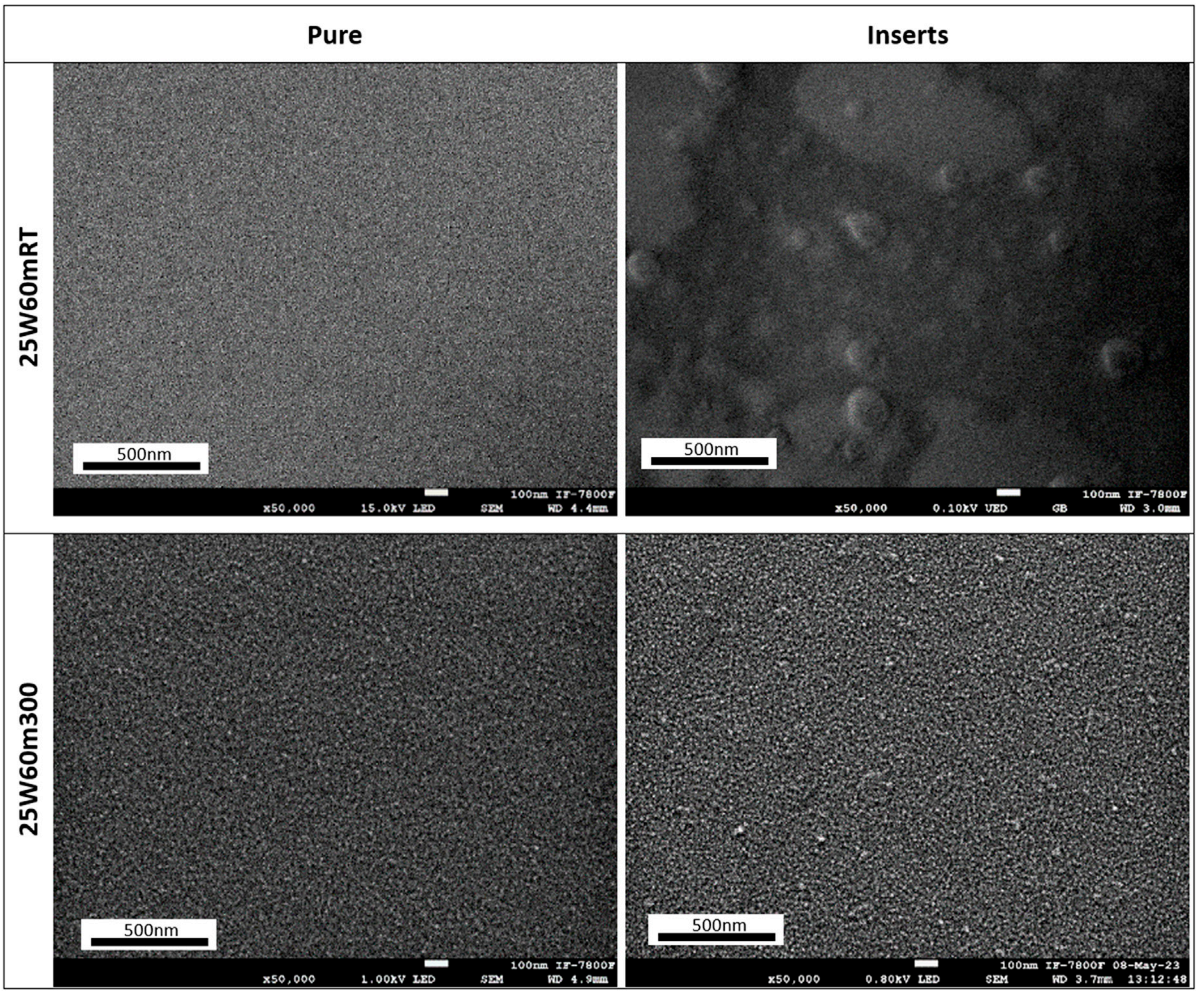

FIGURE 4
SEM micrographs of SiON thin films deposited at 25 W for 60 min under four conditions: pure target at RT, Si-insert target at RT, pure target at 300 °C, and Si-insert target at 300 °C. Pure-target films are smooth and continuous, whereas insert-containing films exhibit protrusions/defects, accentuated at 300 °C, consistent with Si-rich clustering.

rate and the film density. Furthermore, geometric shadowing during deposition can influence the local flux of incoming particles, leading to variations in microstructure across the film. The combined influence of resputtering, geometric shadowing, and microstructural evolution explains why thickness does not scale proportionally with deposition time or power, and why films grown under different plasma conditions exhibit distinct growth regimes rather than a single linear trend.

These findings confirm that film thickness in sputtered SiON is not only a function of deposition time but is also governed by a complex interplay between plasma energy, substrate heating, and compositional modifications of the target. This highlights the importance of optimizing growth conditions to balance thickness control with desired microstructural and optical properties.

3.2.2 Energy dispersive X-ray spectroscopy

Energy Dispersive X-ray Spectroscopy (EDX), integrated into SEM, was employed to quantify the chemical composition of the deposited films. To convert the intensities of the characteristic X-ray peaks into elemental concentrations, correction methods are used that consider physical effects of the sample. The ZAF (Atomic Number, Absorption, and Fluorescence) method applies corrections for the atomic number of the elements, X-ray absorption within the sample, and fluorescence induced by the interaction of X-rays with other atoms. This method is generally performed by comparing the obtained signal with known standards, providing accurate and reliable concentrations. Alternatively, the standardless method allows for estimating the composition without the need for standards, using theoretical models of X-ray generation and general instrument calibrations. The analysis confirmed the presence of nitrogen, oxygen, and silicon in 300 °C samples.

For consistency and comparability, all compositional analyses were performed using an acceleration voltage of 5 kV, which is suitable for the detection of light elements such as oxygen and nitrogen. Measurements were carried out at a working distance of 10 mm using area analyses at ×150 magnification, ensuring representative sampling of the film surface.

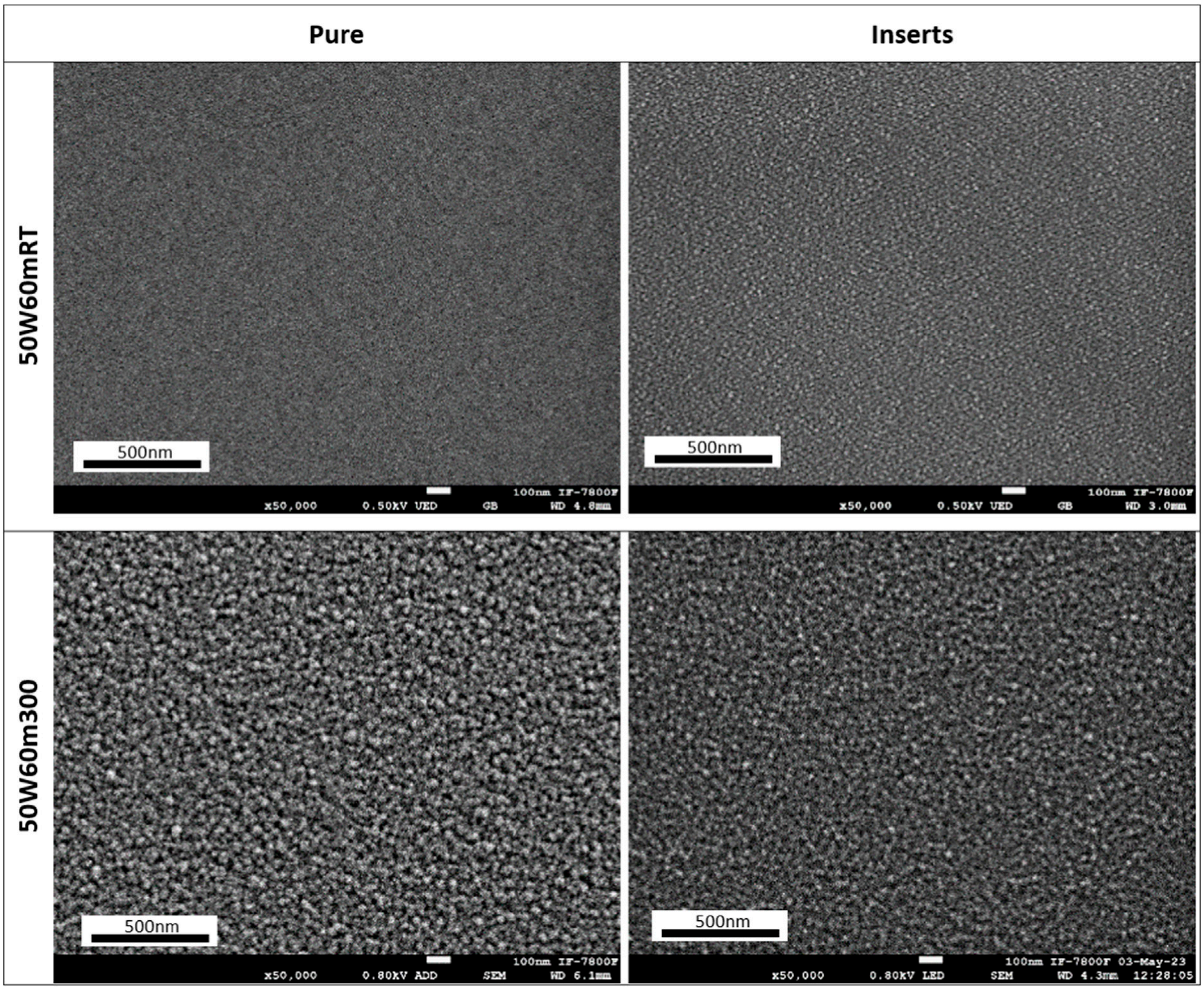

FIGURE 5
SEM micrographs of SiON thin films deposited at 50 W for 60 min (same four conditions and magnifications as Figure 4). Surfaces become more uniformly textured overall; the pure-target series at RT and 300 °C shows the smoothest morphology within the dataset. Insert-containing films remain granular but more homogeneous than at 25 W.

In this study, two complementary EDX measurement techniques were employed: surface analysis (top view) and cross-sectional analysis. Surface EDX was first performed on all samples using an analysis area of 750 × 500 µm, providing an average and representative measurement of the film's surface chemistry. This mode is suitable when the film thickness is large enough for the 5 kV electron beam to remain largely confined within the deposited SiON layer, allowing for reliable quantification without significant contributions from the quartz substrate.

In thin films with thicknesses less than 300 nm, the electronic interaction volume at 5 kV exceeds the film thickness. Under these conditions, the characteristic X-ray emission includes contributions from the substrate, distorting elemental quantification, especially in low-energy lines such as N Kα and O Kα. To overcome this limitation, these thin films were analyzed in cross-section, where the electron beam interacts laterally through the film's thickness rather than penetrating it vertically. This configuration significantly reduces substrate contributions and ensures that the detected X-ray signal originates primarily from the SiON layer.

An example of the cross-sectional EDX analysis is shown in Figure 8 for the representative sample 75W60mRT pure. The EDX line scan was acquired across the film thickness, as indicated by the scan path in the corresponding SEM micrograph. The line scan is included to qualitatively illustrate the presence and spatial distribution of Si, O, and N across the film thickness. Quantitative atomic weight percentages, however, were obtained from area EDX measurements performed under standardized conditions, as described above and summarized in Table 3. The intensity profiles in Figure 8 confirm that the detected X-ray signal originates predominantly from the SiON layer, with minimal contribution from the underlying substrate, and further indicate a continuous, non-stoichiometric SiO_xN_y film dominated by silicon and oxygen.

Elemental compositions reported with one decimal place to reflect the typical accuracy of the technique, particularly for light elements such as N and O, whose quantification is affected by low fluorescence yield and detector efficiency. Compositional profiles revealed a systematic nitrogen deficiency relative to stoichiometric Si_3N_4, accompanied by substantial oxygen incorporation. This

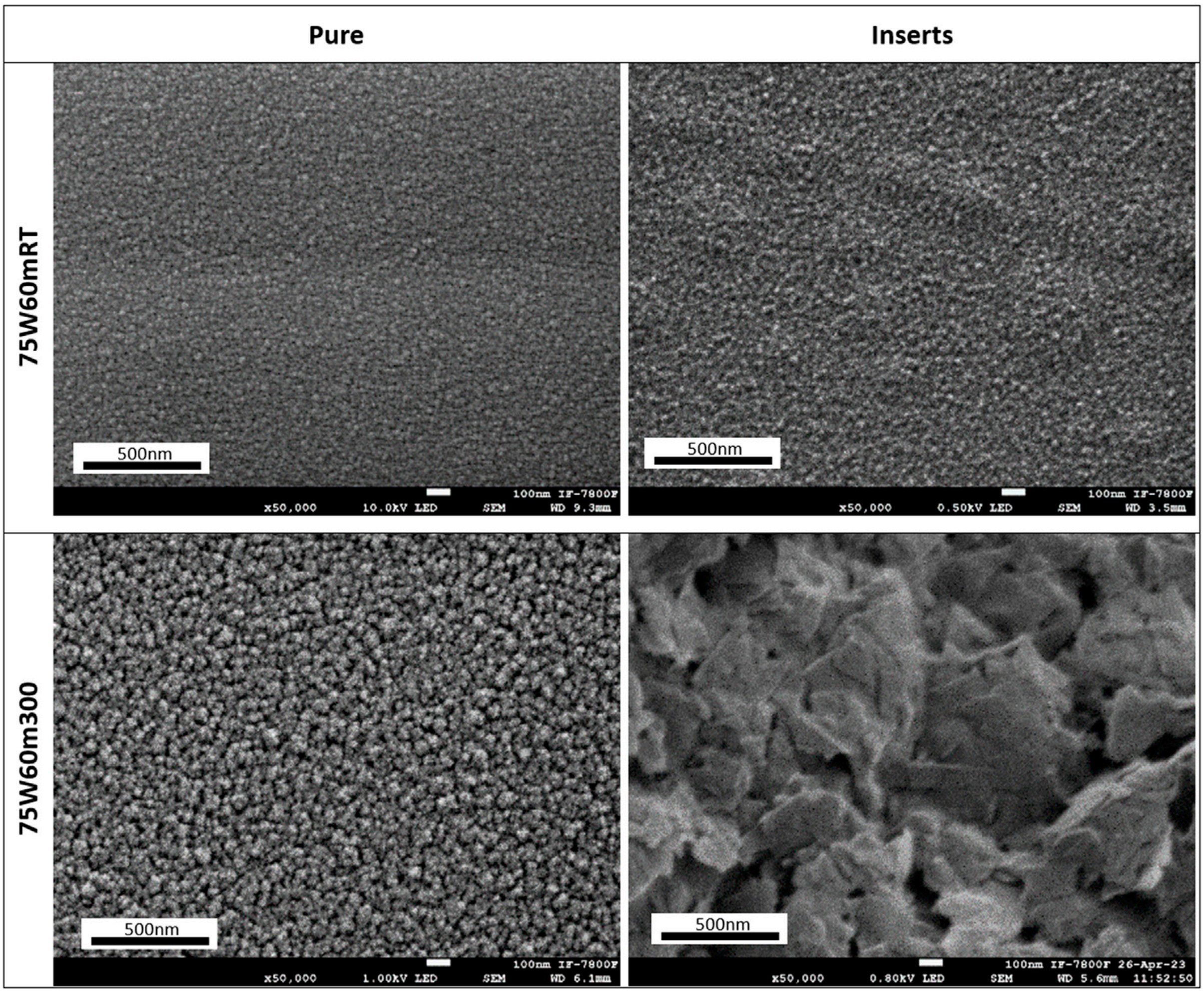

FIGURE 6
SEM micrographs of SiON thin films deposited at 75 W for 60 min (same four conditions and magnifications as Figure 4). Pure-target films remain dense and granular, whereas Si-insert +300 °C produces faceted, flake-like aggregates and pronounced roughening, consistent with a shift toward three-dimensional growth under high Si-rich flux and elevated adatom mobility.

clearly indicates the formation of silicon oxynitride rather than pure nitride, with oxidation of Si playing a dominant role during deposition at 300 °C. Such oxygen enrichment is particularly relevant since it modifies the electronic structure by introducing Si-O bonds and defect-related states within the bandgap, thereby lowering the effective optical gap compared to ideal SiON [43].

Although no oxygen-containing gas was intentionally introduced during deposition, the incorporation of oxygen is fully consistent with known residual gas effects in non-baked sputtering chambers. The substrate heating (up to 300 °C) does not eliminate adsorbed O_2 and H_2O layers from the chamber walls or internal components, which remain significantly cooler than the substrate. When the Ar plasma is ignited, these oxygen-bearing species are desorbed and activated, enabling their incorporation into the growing Si-based film. Silicon's strong affinity for oxygen further facilitates the formation of Si–O bonds even from trace amounts of residual gas.

Processing parameters strongly modulated the final stoichiometry. Both higher RF power and longer deposition times favored increased nitrogen and oxygen uptake, suggesting that more energetic plasma conditions enhance both nitridation and oxidation pathways. The effect of target enrichment with silicon inserts was also evident: films deposited with inserts consistently contained higher oxygen and slightly lower nitrogen contents than those obtained from pure targets. This trend is consistent with the enhanced reactivity of sputtered Si species, which readily form suboxides (SiO_x, $x < 2$) or oxidized nanoclusters during growth, effectively shifting the film composition toward oxygen-rich regimes.

Overall, these results emphasize the high sensitivity of SiON stoichiometry to plasma conditions and target modifications. The observed compositional deviations, –particularly oxygen enrichment and nitrogen deficiency–provide a natural explanation for the reduced optical bandgaps measured in Section 3.7, linking the chemical environment directly to the electronic and optical responses of the films.

To explicitly visualize this relationship, Figure 9 correlates the optical bandgap with the normalized oxygen atomic ratio

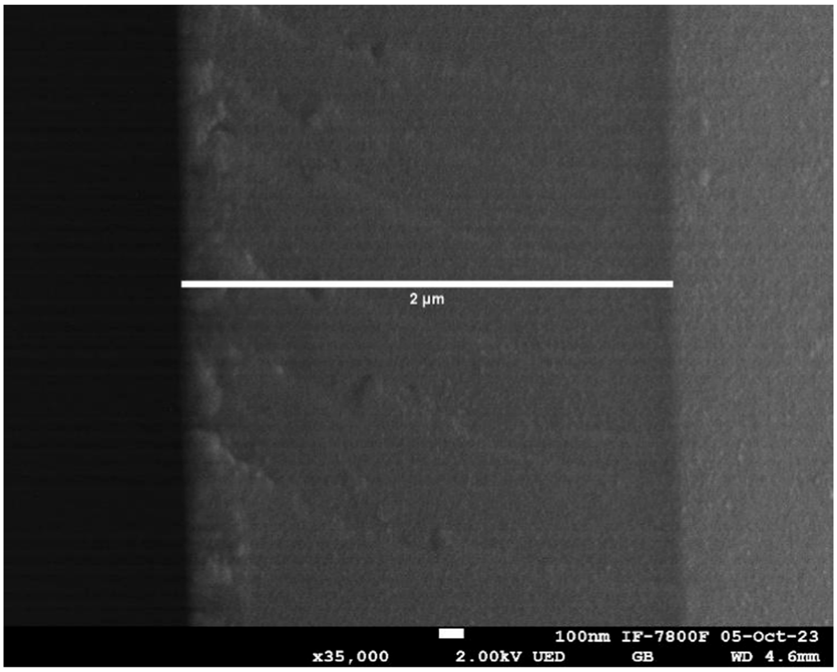

FIGURE 7
Cross-sectional SEM micrograph of a SiON thin film deposited at 75 W for 60 min with silicon inserts at 300 °C. The sample was sectioned using a Buehler Isomet 1,000 precision saw to ensure a clean cut and minimize mechanical damage. The image, acquired at ×35,000 magnification, shows a uniform film thickness of approximately 2 µm, illustrating the effect of target enrichment and substrate heating on growth rate.

O/(O + N) for films deposited at 300 °C. The representation clearly distinguishes nitrogen-rich and oxygen-rich compositions and demonstrates that an increase in oxygen incorporation is systematically associated with bandgap widening. This summary plot provides a direct link between stoichiometry and optical tunability, complementing the compositional trends derived from EDX analysis.

It should be noted that EDX has intrinsic limitations for the quantitative detection of light elements such as nitrogen. The N Kα emission line lies at very low energy (~0.39 keV), where detector efficiency decreases sharply and absorption within the detector window becomes significant. Under these conditions, the nitrogen signal is inherently weak and carries considerably higher uncertainty than the Si and O signals. In addition, the electron interaction volume at the operating beam energies exceeds the film thickness, resulting in partial contributions from the underlying substrate, which further reduces the reliability of N quantification. For these reasons, the nitrogen contents reported here should be interpreted as qualitative or semi-quantitative indicators of compositional trends rather than absolute concentrations.

In this context, X-ray photoelectron spectroscopy (XPS) would be the most appropriate technique for accurate nitrogen quantification and detailed chemical-state analysis (Si–N, Si–O, Si–O–N), given its surface sensitivity and superior capability for detecting light elements. However, XPS measurements were not available in the present study, and EDX was employed to monitor relative variations in composition as a function of deposition parameters. Despite its limitations, EDX still provides consistent trends in N and O incorporations, which remain valuable for correlating plasma conditions with the resulting SiON stoichiometry.

3.3 Transmission electron microscopy (TEM)

High-resolution TEM was employed to investigate the microstructure of SiON thin films deposited by RF-MS at 40 mTorr. The results highlight a strong dependence of morphology and crystallinity on sputtering power, substrate temperature, and target configuration (pure or insert-modified).

At room temperature, films grown from a pure target exhibited predominantly amorphous features with only faint short-range ordering, as shown in Figure 10. Increasing power led to partial nanocrystallization, visible as isolated darker contrast regions. In contrast, the introduction of silicon inserts promoted the segregation of nanometric Si-rich domains, as illustrated in Figure 11, consistent with the nucleation of embedded Si nanoclusters within the amorphous oxynitride matrix. This microstructural signature provides first evidence for phase separation between Si and SiON, a phenomenon strongly favored under non-stoichiometric, oxygen-rich conditions as revealed by EDX.

Increasing RF power led to a transition from porous, amorphous structures (25 W) to more densely packed and homogeneous granular films (75 W). This evolution is attributed to enhanced adatom mobility and kinetic energy at higher powers, improving film compaction and uniformity. Samples

TABLE 2 Average thickness and corresponding deposition rates of SiON thin films deposited by RF-MS, measured from SEM cross-sectional images. Both the film thickness and the deposition rate increase systematically with RF power, deposition time, and substrate heating. The data confirm that target enrichment with silicon promotes higher growth rates compared to pure targets under similar conditions.

Sample	Thickness [nm]	Thickness std dev. [nm]	Rate [nm/min]
25W60mRT inserts	49	6	0.8
25W60m300 inserts	196	30	3.3
25W60m300 pure	42	7	0.7
25W90mRT pure	31	3	0.3
25W90mRT inserts	74	10	0.8
25W90m300 inserts	298	43	3.3
25W90m300 pure	112	11	1.2
25W120mRT pure	270	22	2.3
25W120mRT inserts	369	43	3.1
25W120m300 inserts	763	103	6.4
25W120m300 pure	594	37	4.9
50W30mRT pure	66	6	2.2
50W30mRT inserts	66	9	2.2
50W30m300 inserts	298	43	9.9
50W30m300 pure	119	18	4.0
50W60mRT pure	198	9	3.3
50W60mRT inserts	157	8	2.6
50W60m300 inserts	286	37	4.8
50W60m300 pure	199	7	3.3
75W10mRT pure	15	2	1.5
75W10mRT inserts	51	8	5.1
75W10m300 inserts	61	9	6.2
75W10m300 pure	77	12	7.7
75W30mRT pure	52	2	1.8
75W30mRT inserts	88	6	2.9
75W30m300 inserts	343	46	11.4
75W30m300 pure	175	19	5.8
75W60mRT pure	220	14	3.7
75W60mRT inserts	196	12	3.3
75W60m300 inserts	2000	8	33.3
75W60m300 pure	393	45	6.5

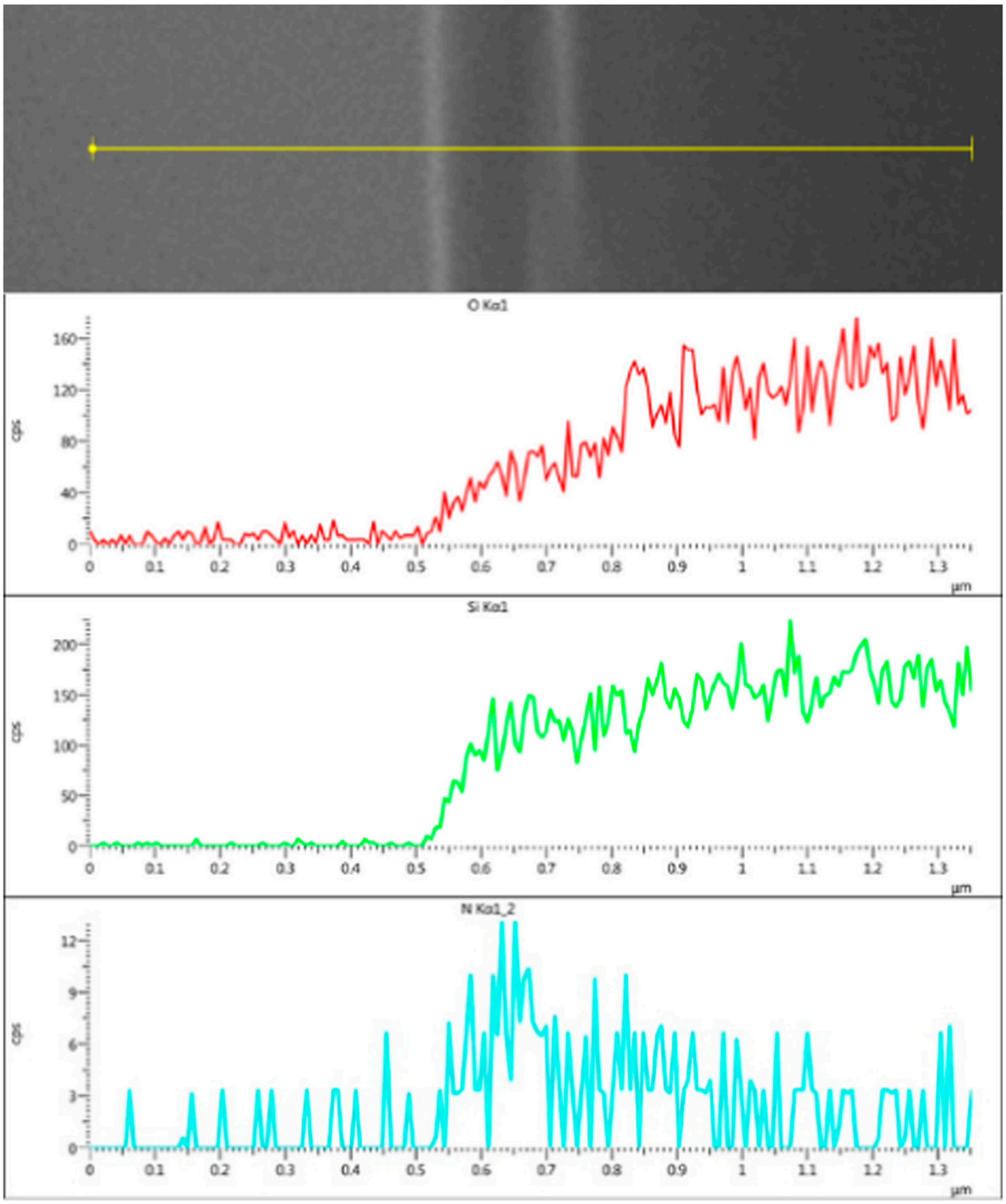

FIGURE 8
Cross-sectional SEM image and corresponding EDX line scan of the 75W60mRT pure SiON thin film deposited by RF sputtering using a Si_3N_4 target enriched with silicon inserts. The yellow line indicates the scan path across the film thickness. The EDX line scan is included for qualitative illustration of the spatial distribution of Si, O, and N across the film thickness only. The intensity profiles demonstrate that the detected X-ray signal originates predominantly from the SiON layer, with minimal contribution from the underlying substrate.

grown with pure targets consistently showed higher crystallinity and structural uniformity compared to those deposited using inserts, which often exhibited localized defects or compositional variations.

The observed transition from amorphous to nanocrystalline morphologies with power underscores the kinetic control of nucleation and growth processes in sputtered SiON. Importantly, the presence of discrete Si-rich nanodomains suggests that the films can host quantum-dot-like inclusions capable of influencing optical absorption and emission, in agreement with the reduced bandgap values reported in Section 3.7.

3.3.1 Indexing of TEM diffraction patterns

The indexing of diffraction features, and consequently the identification of crystalline phases and zone axes, was systematically performed by measuring interplanar distances from the micrographs and comparing them with reference X-ray diffraction tables for Si [44] and Si_3N_4 [45].

TABLE 3 Atomic weight percentages of N, O, and Si in thin films deposited by RF-MS at 300 °C, determined by EDX integrated into SEM. The films exhibit nitrogen deficiency and significant oxygen incorporation relative to stoichiometric Si_3N_4, consistent with the formation of non-stoichiometric silicon oxynitride. Target enrichment with silicon inserts generally increased oxygen uptake and reduced nitrogen content, indicating that deposition conditions critically influence the final composition.

ID	N wt. [%]	O wt. [%]	Si wt. [%]	σ N wt. [%]	σ O wt. [%]	σ Si wt. [%]
25W60m300 pure	2.1	9.3	88.6	0.5	0.4	0.6
25W60m300 inserts	1.3	9.3	89.5	0.2	0.2	0.3
25W120m300 pure	8.7	25.8	65.4	0.6	0.5	0.6
25W120m300 inserts	8.1	36.8	55.2	0.4	0.5	0.6
50W30m300 pure	10.5	15.6	73.9	0.7	0.5	0.8
50W30m300 inserts	3.9	22.5	73.6	0.3	0.4	0.5
50W60m300 pure	22.2	24.5	53.3	0.9	0.7	0.9
50W60m300 inserts	17.4	32.2	50.4	0.5	0.5	0.6
75W30m300 pure	21.5	23.7	54.8	0.9	0.7	0.9
75W30m300 inserts	21.8	30.4	47.8	0.5	0.5	0.6

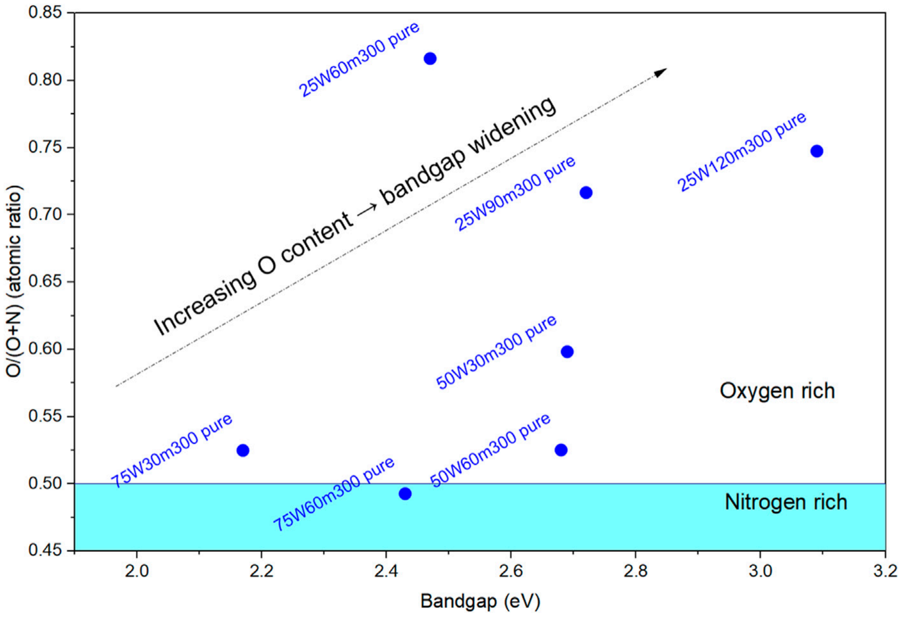

FIGURE 9
Relationship between optical bandgap and normalized oxygen atomic ratio O/(O + N) for SiON thin films deposited at 300 °C using pure Si_3N_4 targets. The horizontal line at O/(O + N) = 0.5 separates nitrogen-rich and oxygen-rich compositions. An increase in bandgap is observed with increasing oxygen incorporation, indicating that stoichiometry plays a central role in tuning the optical properties of RF-sputtered SiON films.

Selected-area electron diffraction (SAED) patterns evidenced a clear structural evolution with sputtering power, as shown in Figure 12. At 25 W, Figure 12b displays broad diffuse halos consistent with amorphous SiON, though weak reflections corresponding to hexagonal Si_3N_4 with planes (201) and (330), oriented along the $[\bar{3}26]$ zone axis, were also detected. Increasing the power to 50 W, Figure 12d reveals sharp diffraction rings and spots, confirming a polycrystalline arrangement combining face-centered cubic Si (111) with hexagonal Si_3N_4, where planes (200), (201), and (301) were distinguished. At 75 W, Figure 12f shows a more defined pattern, with planes (200) and (114) oriented along the $[4\ \bar{8}\ 3]$ zone axis at an inclination of ~88°, reflecting enhanced crystallinity and the growth of larger Si nanocrystals.

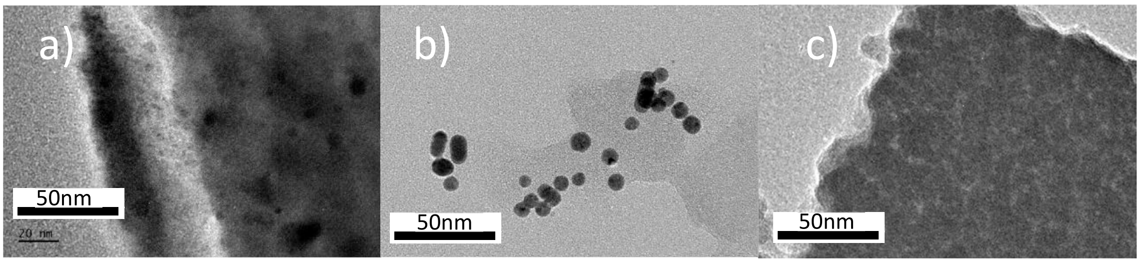

FIGURE 10
200kX micrographs of films grown at RT Using a Pure Target for 60 min at Various Power Levels: **(a)** 25 W, **(b)** 50 W, **(c)** 75 W.

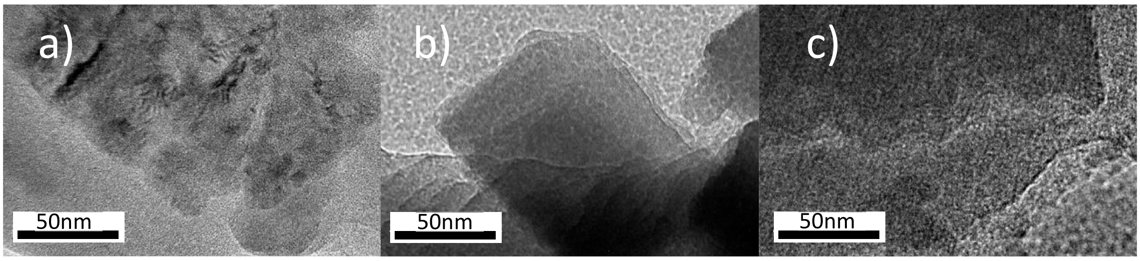

FIGURE 11
200kX micrographs of films grown at RT Using an Insert-Modified Target for 60 min at Various Power Levels: **(a)** 25 W, **(b)** 50 W, **(c)** 75 W.

This coexistence of crystalline Si and Si_3N_4 phases provides compelling evidence for the nucleation of excess sputtered Si as nanocrystals within the oxynitride network. Such embedded Si nanoclusters behave as quantum dots confined in the nitride host, accounting for the microstructural heterogeneity observed in Figures 10, 11 and offering a microscopic origin for the reduced optical bandgap (2.17–3.09 eV) and the quantum confinement effects discussed in Section 3.7.

3.4 Atomic force microscopy

Surface roughness is a critical parameter in thin film research, as it directly influences light scattering, carrier mobility, and interface quality, thereby impacting the performance of optoelectronic and dielectric devices. Atomic Force Microscopy (AFM) provides high-resolution topographical data that allow quantitative evaluation of nanoscale morphology. Figure 13 shows representative 2D and 3D AFM topography images of the 25W60m300 inserts sample, revealing a heterogeneous surface with peak-to-valley variations of ~17 nm.

The complete set of root-mean-square (RMS) roughness values is presented in Table 4. A clear dependence on sputtering power, substrate temperature, and the use of silicon inserts can be distinguished. At room temperature, roughness values remain moderate, but the addition of silicon inserts consistently increases surface irregularities, for example from 2.29 nm to 3.25 nm at 25 W, and from 3.82 nm to 4.97 nm at 50 W. At 300 °C, the evolution becomes more pronounced: while films deposited at 25 W from a pure target exhibit exceptionally smooth surfaces (~0.94 nm), the inclusion of inserts doubles the roughness to ~2.22 nm. At higher power and elevated temperature, roughness increases dramatically, reaching values as high as 9.20 nm for the 75W60m300 inserts sample.

These trends indicate that both RF power and substrate heating enhance adatom mobility and surface diffusion, promoting the coalescence of islands and the formation of Si-rich clusters. The resulting morphology, characterized by more pronounced nanoscale features, directly correlates with the optical absorption and scattering behavior observed in subsequent sections. Thus, AFM analysis confirms that the interplay between deposition energy and target enrichment governs the balance between smooth, dielectric-like films and rougher surfaces enriched with nanostructured domains.

3.5 Optical absorption and bandgap determination

The optical response of the silicon oxynitride thin films was evaluated through the absorption coefficient (α) as a function of photon energy, which provides more direct insights into electronic transitions than raw absorbance or transmittance spectra. The film thicknesses were determined from cross-sectional SEM measurements, showing that the thickness increases with increasing deposition power. In order to analyze how the absorption coefficient is modified, it is important to recall that the absorbance is related to the transmittance according to $A = -log_{10}(T)$.

The transmittance can be expressed as, $T = e^{-\alpha t}$ where α is the absorption coefficient and t is the film thickness. Since both

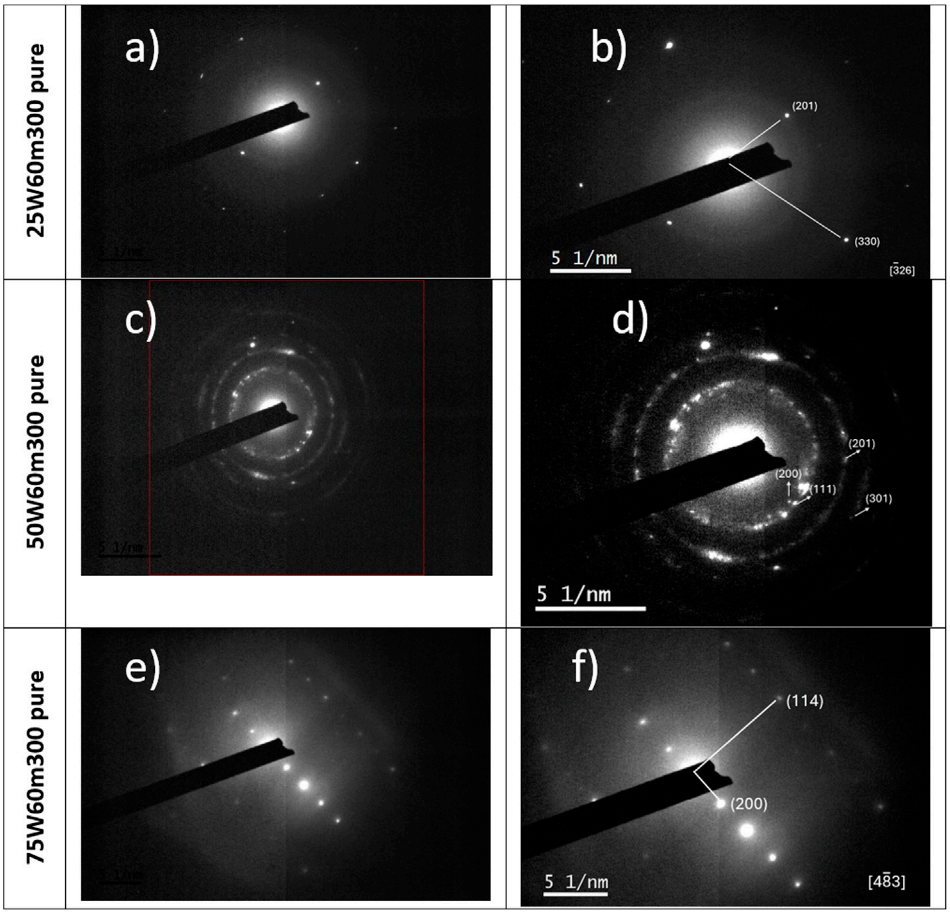

FIGURE 12
Selected-area electron diffraction (SAED) patterns and indexing of SiON thin films deposited at 300 °C under different sputtering powers: **(a,b)** 25 W, **(c,d)** 50 W, and **(e,f)** 75 W. At 25 W, diffuse halos indicate a predominantly amorphous matrix with weak reflections of hexagonal Si_3N_4. At 50 W, sharp rings and spots confirm a polycrystalline structure with coexistence of cubic Si and hexagonal Si_3N_4. At 75 W, stronger reflections such as (200) and (114) evidence enhanced crystallinity and the growth of larger Si nanocrystals within the oxynitride matrix.

the thickness and the transmittance are known, the absorption coefficient can be determined as a function of the photon energy, which is then used for the Tauc analysis.

In the case of amorphous and polycrystalline materials, the Tauc method is employed to obtain an accurate estimation of the optical bandgap. This methodology relies on the fact that optical transitions between the valence and conduction bands are enhanced by structural disorder. Consequently, the Tauc approach is widely regarded as a reliable method for determining the optical bandgap in amorphous and polycrystalline semiconductors, particularly those based on silicon.

The Tauc optical gap is calculated using the expression:

$$\alpha(E) = B\frac{(E - E_{OP})^2}{E}$$

where $\alpha(E)$ is the absorption coefficient at a given photon energy, E_{op} represents the optical bandgap of the material, and B is the Tauc slope constant.

Figures 14, 15 display the absorption behavior of films deposited under different sputtering conditions, evidencing a strong dependence on deposition parameters.

At room temperature and 50 W, the use of silicon inserts leads to a marked increase in α across the entire spectral range, indicating higher optical losses and reduced transparency. This effect becomes even more pronounced at elevated temperatures, where films deposited at 300 °C show systematically higher α values with increasing sputtering power. Importantly, this trend cannot be attributed to thickness effects, since the absorption coefficient intrinsically normalizes the film thickness and constitutes a fundamental property of the material. Instead, the observed increase reflects microstructural and electronic modifications induced by higher power and temperature, such as enhanced film densification, structural disorder, and the introduction of localized states that raise the probability of optical transitions.

The optical bandgap was subsequently determined from the absorption coefficient using the Tauc method for indirect semiconductors (n = 2), which is particularly suitable for amorphous and disordered silicon-based systems. Figure 16 illustrates the Tauc plot for the 75W60m300 pure sample, from which the linear extrapolation of $(\alpha\ h\nu)^{1/2}$ versus photon energy yields the bandgap value. Table 5 summarizes the calculated bandgaps for films deposited at 300 °C under varied sputtering conditions.

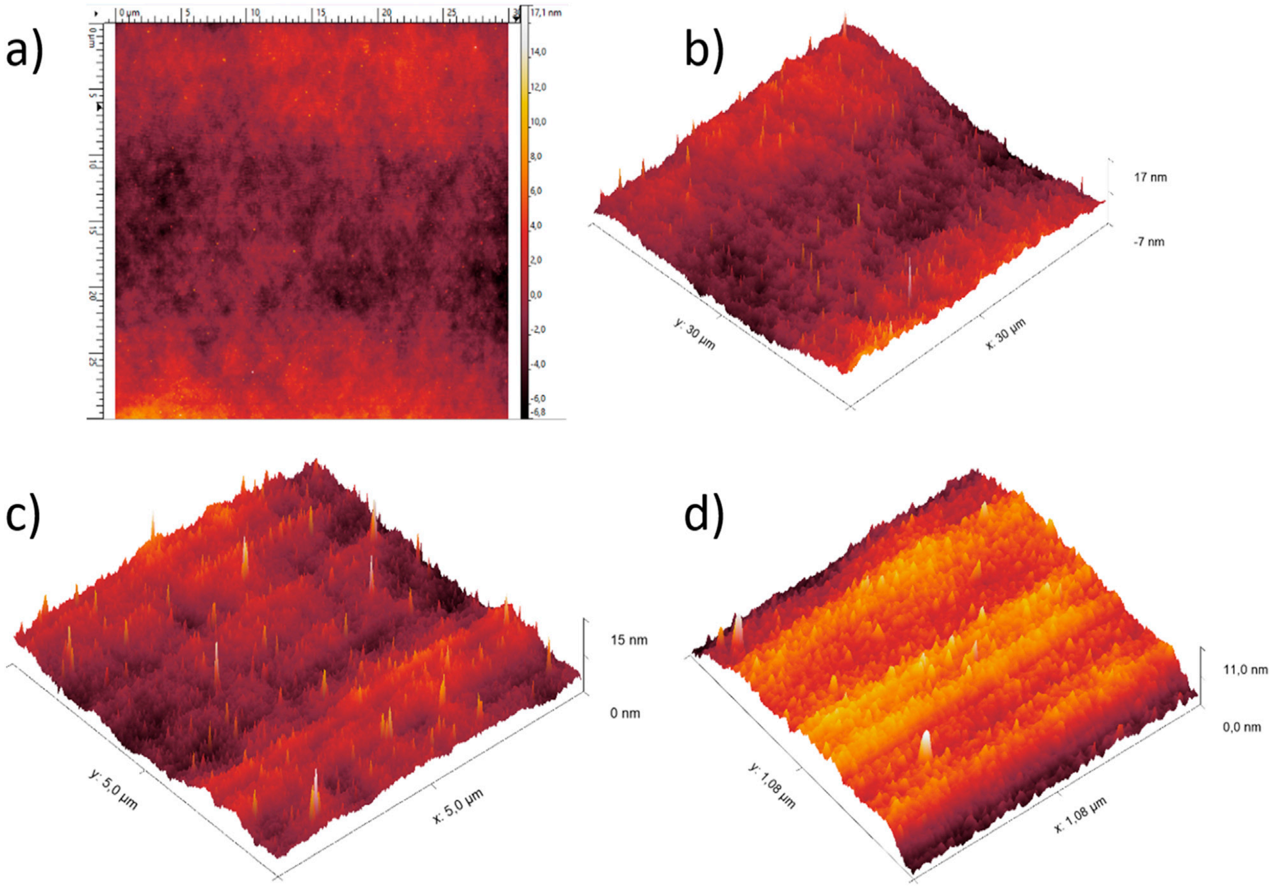

FIGURE 13
Two-dimensional **(a)** and three-dimensional **(b–d)** AFM topography images of a SiON thin film deposited at 25 W for 60 min at 300 °C using silicon inserts. The scanned area **(a,b)** 30 × 30 μm^2, **(c)** 5 × 5 μm^2 and **(d)** 1 × 1 μm^2 reveals a heterogeneous morphology with peak-to-valley height variations of ~17 nm, indicative of enhanced surface diffusion and cluster formation under these growth conditions.

The results reveal that the bandgap values span the range 2.2–3.1 eV, placing the films within the optical window relevant for both visible and ultraviolet applications. A general trend is observed in which longer deposition times produce wider bandgaps at low (25 W) and high (75 W) powers, while films grown at intermediate power (50 W) maintain relatively stable values, suggesting a more homogeneous growth regime. The bandgap values can be grouped into two categories: above 2.5 eV, suitable for ultraviolet applications such as UV/blue light-emitting diodes; and below 2.5 eV, more appropriate for visible-spectrum devices including sensors and photocatalytic coatings.

Together, the absorption coefficient and bandgap analysis demonstrate that sputtering parameters exert a dual influence: they control the structural compactness and disorder that determine optical losses, while simultaneously tuning the electronic structure responsible for photon absorption and bandgap modulation. This interplay highlights the potential of SiON thin films as a versatile material platform, where deposition conditions can be deliberately tailored to engineer optical performance for targeted optoelectronic applications.

The uncertainties associated with the thickness and roughness measurements do not affect the robustness of the optical analysis. Thickness variations introduce only a uniform shift in the absorption magnitude, without modifying the spectral shape or the position of the absorption edge; therefore, the extracted bandgap values remain unchanged. Similarly, the measured roughness values are negligible compared to the probing wavelengths, implying that any additional scattering is minimal and spectrally uniform. Overall, these sources of uncertainty fall within the expected range for sputtered films and do not influence the observed optical trends or the conclusions drawn from the optical analysis.

3.6 Ellipsometry

The refractive indices of the deposited films were determined by monochromatic null ellipsometry using a 632 nm laser at an incidence angle of 70°. In the ellipsometric analysis, the film thickness was not treated as a free fitting parameter. Instead, thickness values obtained from SEM cross-sectional measurements (Table 2) were used as fixed input parameters in the optical model. The analyzed films span a wide thickness range, from approximately 30 nm up to 2 µm, depending on the deposition conditions.

TABLE 4 Root-mean-square (RMS) roughness values of SiON thin films measured by AFM under varied sputtering conditions. Roughness systematically increases with RF power and substrate temperature, with silicon inserts consistently promoting higher surface irregularities. These results confirm that energy input and target modification strongly modulate nanoscale morphology.

Sample	Roughness [nm]
25W60mRT pure	2.29
25W60mRT inserts	3.25
25W60m300 pure	0.94
25W60m300 inserts	2.22
50W60mRT pure	3.82
50W60mRT inserts	4.97
50W60m300 pure	4.78
50W60m300 inserts	6.80
75W30m300 inserts	6.80
75W60mRT pure	1.95
75W60mRT inserts	1.88
75W60m300 pure	4.14
75W60m300 inserts	9.20

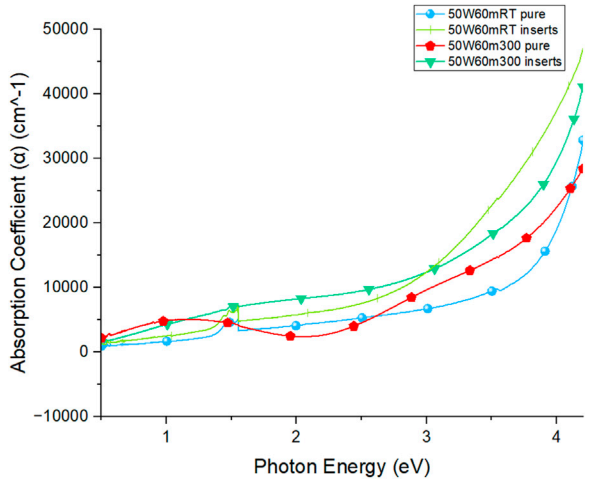

FIGURE 14
Absorption coefficient of thin films grown on a quartz substrate at 50 W for 60 min with variations in temperature and target composition.

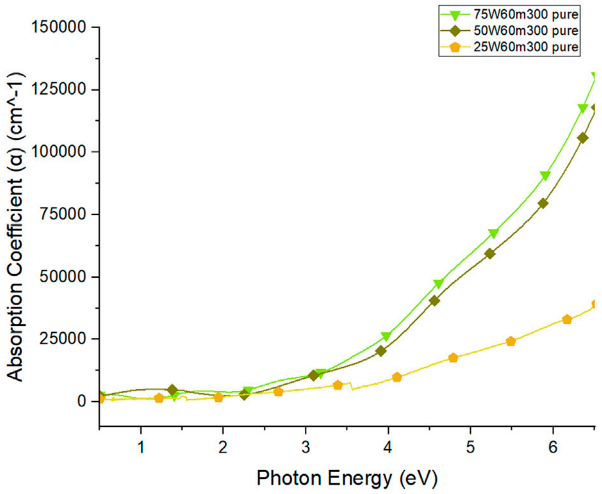

FIGURE 15
Absorption coefficient of thin films grown on a quartz substrate at 300 °C for 60 min, with variations in sputtering power (25, 50, and 75 W) and target composition.

In monochromatic null ellipsometry, the polarizer and analyzer are adjusted to achieve a minimum reflected intensity condition, allowing the determination of the ellipsometric parameters Ψ and Δ. The parameter Ψ corresponds to the relative amplitude change between the p and s polarized components of the reflected beam, while Δ represents the phase shift introduced between these components during reflection. From these parameters, the optical equations for an isotropic thin film were solved to obtain the refractive index n at 632 nm.

Since the measurement was performed at a single wavelength, the analysis was carried out using a monochromatic isotropic optical model, suitable for dielectric films with negligible absorption in this spectral region ($k \approx 0$). This approach differs from the dispersion models commonly used in spectroscopic ellipsometry, such as Cauchy or Tauc-Lorentz, which require measurements at multiple wavelengths. In monochromatic null ellipsometry, the optical constants are determined directly at the selected wavelength without fitting a spectral dispersion curve. Therefore, the reported refractive index values correspond exclusively to the response at 632.8, and no spectral dispersion over a broader wavelength range was analyzed.

The wavelength of 632.8 nm was used due to the high stability and coherence of the laser and the low absorption of SiON films in this region of the visible spectrum. These conditions improve the accuracy of the refractive index determination.

The incidence angle of 70° was selected because of its proximity to the Brewster angle for materials with refractive indices in the range of 1.3–2.2, thus maximizing the sensitivity of Ψ and Δ to variations in the film's optical properties. In this study, ellipsometric measurements were performed only at this incidence angle, and no additional angles were evaluated.

The results, summarized in Table 6, span a wide range from 1.41 to 2.11, values that fall within the typical window for silicon oxynitride thin films, which extends from ~1.44 for SiO_2 to ~2.05 for Si_3N_4.

The refractive index values are reported with two decimal places. Considering the stability of the He–Ne laser, the selected incidence angle close to the Brewster condition, and the negligible absorption of the films in this spectral region, the uncertainty in n is estimated to be on the order of ±0.01–0.02, justifying the reported precision.

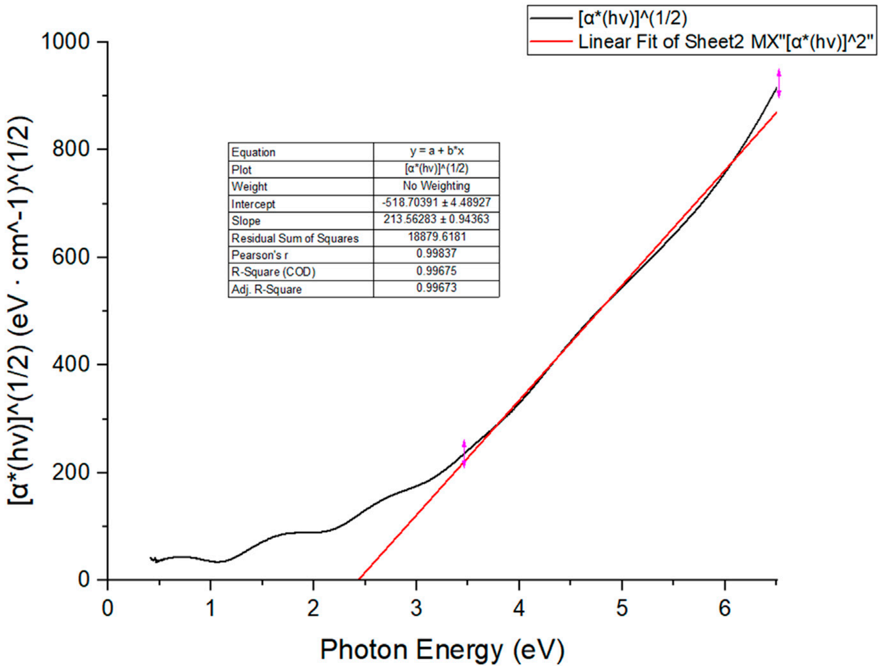

FIGURE 16
Tauc plot for the determination of the band gap energy of the 75W60m300 pure sample.

TABLE 5 Bandgap values calculated by the Tauc method for indirect semiconductors in thin films grown at 300 °C with pure silicon oxynitride targets.

Sample	Bandgap [eV]
25W60m300 pure	2.47
25W90m300 pure	2.72
25W120m300 pure	3.09
50W30m300 pure	2.69
50W60m300 pure	2.68
75W30m300 pure	2.17
75W60m300 pure	2.43

This variation in refractive index reflects the compositional diversity of the samples, consistent with the EDX results that evidenced different proportions of nitrogen and oxygen. Films with higher oxygen content approach the lower end of the index range, closer to silica, while those richer in nitrogen display values nearer to stoichiometric silicon nitride. In this sense, the refractive index can be regarded as a sensitive fingerprint of the film's chemical environment and bonding configuration.

A clear correlation also emerges between refractive index and optical bandgap: samples with wider gaps tend to exhibit lower indices, whereas films with narrower gaps show higher values. This inverse trend is typical of amorphous semiconductors and oxynitride systems, further validating the internal consistency of the optical characterization.

From a technological perspective, the ability to tune the refractive index across such a broad interval highlights the potential of RF-MS SiON films for optoelectronic applications. Precise control of n is crucial for designing dielectric layers, antireflection coatings, and optical waveguides, where both transparency and refractive contrast dictate device performance.

3.7 Photoluminescence

Photoluminescence (PL) measurements were carried out using a 25 mW He-Cd laser at 325 nm as the excitation source, incident on the film surface at 45°, and the emitted light was collected with a Fluoromax-Spex spectrofluorometer through a 1-m optical fiber positioned at 90° relative to the film normal. All spectra were acquired at room temperature under dark-room conditions.

The PL spectra of the films deposited for 60 min at 300 °C using a pure Si_3N_4 target presented in Figure 17 revealed a pronounced emission peak centered at ~3.2 eV (≈390 nm), accompanied by a broader and less intense band extending toward ~2.9 eV. The presence of these features indicates the occurrence of radiative recombination centers within the films. At this stage, it is important to note that the observed photoluminescence can be explained by two main mechanisms: (i) radiative recombination associated with nanoscale silicon-rich regions or nanoclusters, giving rise to possible quantum-confinement-related effects, and (ii) emission originating from intrinsic defect states within the oxynitride matrix.

One plausible interpretation is the formation of silicon nanoclusters embedded in the oxynitride matrix. In this scenario,

TABLE 6 Refractive indices of SiON thin films deposited by RF-MS, measured by null ellipsometry at 632 nm and 70° incidence. The values, ranging from 1.41 to 2.11, cover the typical interval between SiO_2 (~1.44) and Si_3N_4 (~2.05), reflecting compositional variations from oxygen-rich to nitrogen-rich regimes and evidencing the tunability of the optical response.

Sample	Refractive index
25W90mRT pure	2.00
25W120mRT pure	1.73
50W30mRT pure	1.55
50W60mRT pure	1.88
75W10mRT pure	2.00
75W30mRT pure	1.58
75W60mRT pure	2.11
25W60mRT inserts	1.70
25W90mRT inserts	1.62
25W120mRT inserts	1.64
50W30mRT inserts	1.68
50W60mRT inserts	1.68
75W10mRT inserts	1.57
75W30mRT inserts	1.63
75W60mRT inserts	2.00
25W60m300 inserts	2.00
25W90m300 inserts	1.69
25W120m300 inserts	1.70
50W30m300 inserts	1.63
50W60m300 inserts	1.98
75W10m300 inserts	1.52
75W30m300 inserts	1.79
75W60m300 inserts	1.97
25W60m300 pure	1.41
25W90m300 pure	1.62
25W120m300 pure	1.60
50W30m300 pure	1.80
50W60m300 pure	2.00
75W10m300 pure	1.61
75W30m300 pure	2.00
75W60m300 pure	1.90

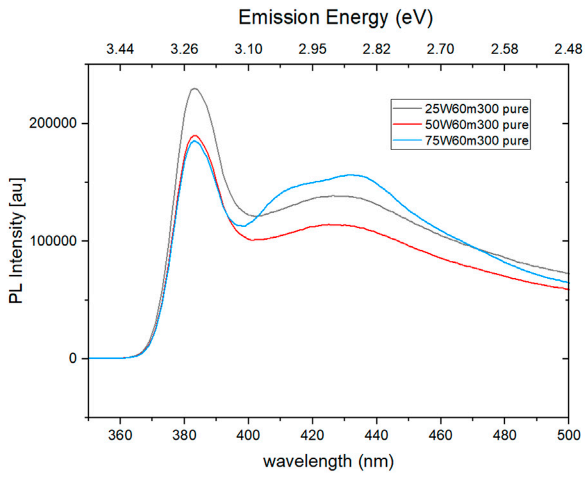

FIGURE 17
Photoluminescence spectra of samples deposited at 300 °C with a pure target for 60 min.

excess sputtered silicon undergoes nucleation and confinement within the amorphous nitride network, giving rise to size-dependent electronic states. Radiative recombination across these confined states would account for the sharp high-energy PL band, while the broader low-energy contribution could be associated with interfacial recombination and structural disorder. The observation of granular features in the HRTEM micrographs of Figure 18 lends partial support to this hypothesis, suggesting the presence of nanoscale inhomogeneities of about 2 nm diameter that could act as quantum dots (QDs) under confinement conditions.

However, an alternative explanation must also be considered. The emission peak at ~3.2 eV is consistent with well-documented defect-related luminescence in SiON and Si_3N_4, arising from oxygen-deficient centers (ODCs), N-Si-O complexes, or dangling bonds [46]. Such defect states frequently produce sharp emission features in the near-UV/blue spectral region, even in the absence of nanocrystalline phases. This interpretation is particularly relevant here, given that the deposition temperature of 300 °C and the absence of post-deposition annealing make the spontaneous formation of sub-2 nm, well-passivated silicon nanocrystals less likely. Furthermore, a definitive attribution to QDs would require complementary structural and chemical evidence from techniques such as EELS, XPS, Raman spectroscopy, or detailed FFT-HRTEM with size-distribution statistics.

In light of the considerations discussed above, the origin of the PL signal is most consistently interpreted by considering both structural and electronic contributions. These findings highlight the complexity of disentangling QD-related luminescence from defect-related processes in silicon oxynitride systems, underscoring the need for complementary structural and spectroscopic analyses to conclusively identify the nature of the emission centers.

While the individual PL spectra provide insight into emission features and recombination mechanisms, a comparative representation is required to identify global trends driven by growth parameters. To this end, Figure 19 summarizes the dependence of

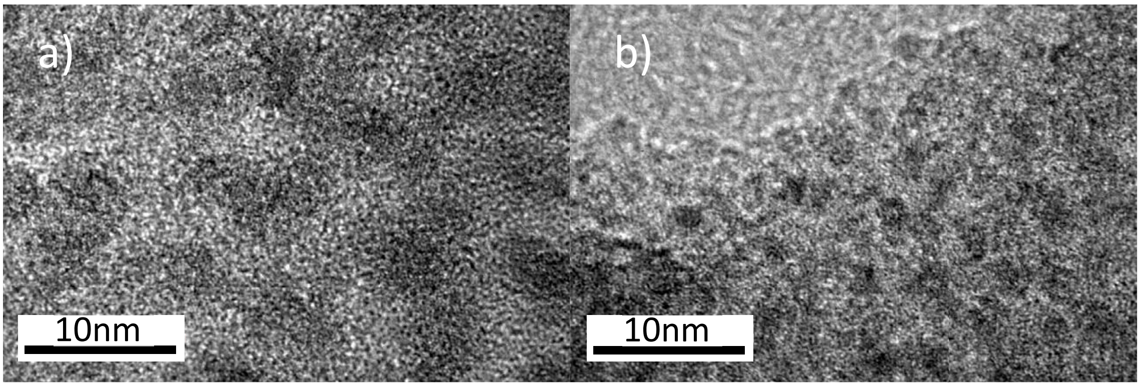

FIGURE 18
Micrographs of films grown for 60 min with a pure target at 300 °C: **(a)** 25 W and **(b)** 50 W.

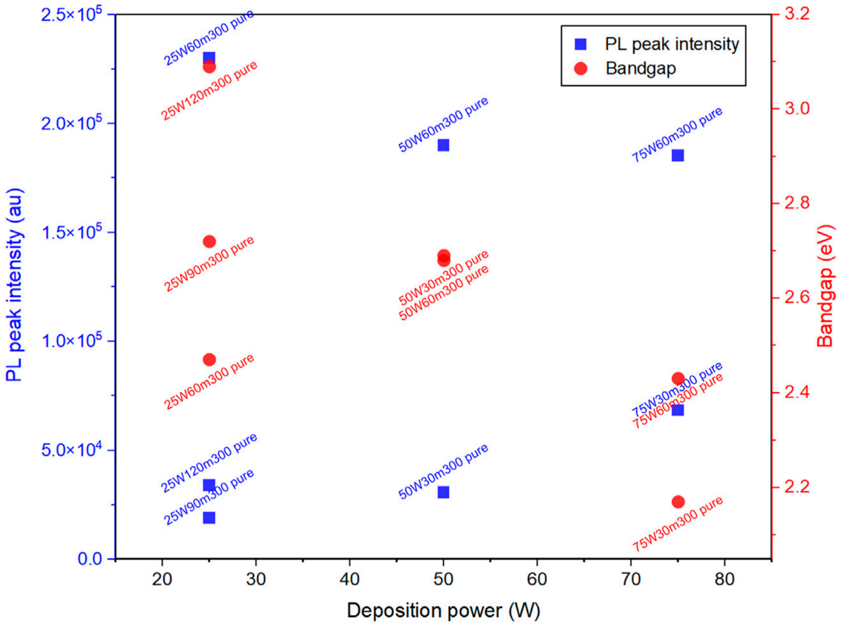

FIGURE 19
Correlation between RF-MS power and optical properties of SiON thin films deposited at 300 °C from a pure Si_3N_4 target. The left axis shows the photoluminescence (PL) peak intensity, while the right axis corresponds to the effective optical bandgap extracted from Tauc analysis. Increasing RF-MS power leads to a systematic reduction of the bandgap and non-monotonic variations in PL intensity, evidencing the tunability of the optical response through plasma energy and growth kinetics.

both the effective optical bandgap and the PL peak intensity on the RF sputtering power for films deposited at 300 °C.

The PL response, however, is non-monotonic: maximum PL intensity occurs at intermediate conditions and does not coincide with the minimum bandgap. This behavior indicates competing radiative and non-radiative pathways, suggesting that emission efficiency is governed by a balance between defect-related radiative centers and quenching mechanisms associated with excessive disorder or clustering.

Finally, our ability to tune the optical and morphological properties of SiON thin films deposited by RF magnetron sputtering using both pure and Si-enriched Si_3N_4 targets enables access to distinct material regimes that are directly relevant to specific device applications. The refractive index values obtained in this work ($n \approx 1.41–2.11$) are consistent with those reported for SiO_xN_Y and related silicon-based films deposited by sputtering and plasma-assisted techniques, spanning the optical window between stoichiometric SiO_2 and Si_3N_4 and confirming access to oxygen-rich, intermediate, and nitrogen-rich regimes.

High-refractive-index films (n up to ~2.1) with low surface roughness (RMS ≈ 1–2 nm), particularly obtained at high RF power under non-enriched conditions (e.g., 75 W, room temperature, 60 min), are well suited for integrated optical waveguides and antireflection coatings, in agreement with recent literature [47].

In contrast, Si-rich films deposited using Si-enriched targets exhibit increased roughness and strong photoluminescence centered around ~3.0 eV (e.g., 50 W, 300 °C, 60 min, with inserts), making them promising candidates for quantum-dot- or defect-based light-emitting layers, consistent with reports on nanostructured silicon systems [47].

The optical bandgaps measured here (2.17–3.09 eV) are significantly lower than those of near-stoichiometric SiON but are fully consistent with previously reported values for silicon-rich and non-stoichiometric oxynitride films, where oxygen incorporation, nitrogen deficiency, and defect-related states narrow the effective gap. Finally, smooth films with moderate refractive index are attractive as dielectric or passivation layers for CMOS-compatible electronics and FET-based biosensors [48]. The observed inverse correlation between refractive index and optical bandgap agrees with established structure–property relationships in amorphous silicon-based materials, confirming that the optical tunability achieved here arises from controlled variations in stoichiometry and bonding enabled by the insert-assisted RF sputtering approach.

4 Conclusion

In this study, we demonstrated that RF-MS of Si_3N_4 targets, modified or not with silicon inserts, enables the growth of non-stoichiometric silicon oxynitride thin films with highly controllable optical, structural, and morphological properties. The effective bandgap was tuned from 2.17 to 3.09 eV and the refractive index from 1.41 to 2.11, evidencing the strong dependence on chemical composition, substrate temperature, and RF power.

Cross-sectional SEM confirmed the growth of compact and dense films, with thicknesses reproducibly scaling up to the micrometer range under high-power and high-temperature conditions. Consistently, RMS roughness values determined by AFM were low in several cases (on the order of 1–3 nm in optimal regimes), which is particularly favorable for the integration of these films into waveguides and high-quality optoelectronic devices where surface scattering must be minimized.

Electron diffraction analysis with systematic indexing revealed both silicon oxynitride phases and pure crystalline silicon domains. The latter correlates with the spontaneous formation of confined nanoclusters likely contributing to the photoluminescence emission centered at 3.2 eV, suggesting quantum-dot-like behavior within the SiON matrix. Nonetheless, an alternative explanation involving radiative recombination through intrinsic defects (such as ODCs, N-Si-O complexes, or dangling bonds) must also be considered, as these centers are well known to produce near-UV emission in silicon oxynitride systems.

Our results established that the strategy based on controlled target modification, systematic tuning of sputtering parameters, and detailed structural analysis provides a reproducible route for the engineering of silicon oxynitride films. This approach enables adjustable optical properties and the potential self-formation of silicon quantum domains or defect-mediated emission centers, opening new opportunities in the design of high-performance photonic and optoelectronic devices.

Data availability statement

The original contributions presented in the study are included in the article/supplementary material, further inquiries can be directed to the corresponding author.

Author contributions

LG-G: Conceptualization, Data curation, Formal Analysis, Investigation, Methodology, Software, Validation, Writing – original draft, Writing – review and editing. AP-M: Conceptualization, Formal Analysis, Investigation, Methodology, Project administration, Resources, Supervision, Validation, Visualization, Writing – original draft, Writing – review and editing. AL-S: Data curation, Formal Analysis, Investigation, Methodology, Supervision, Visualization, Writing – original draft. MA-D-V: Data curation, Investigation, Methodology, Writing – original draft, Writing – review and editing. AR-G: Conceptualization, Data curation, Formal Analysis, Funding acquisition, Investigation, Methodology, Project administration, Resources, Supervision, Validation, Writing – original draft, Writing – review and editing.

Funding

The author(s) declared that financial support was received for this work and/or its publication. This research was funded by PAPIIT-UNAM grant number IN111723 and CONACYT - Apoyos para Adquisición y Mantenimiento de Infraestructura en Instituciones y Laboratorios de Investigación Especializada 2019, grant number: 299881.

Acknowledgements

The first author gratefully acknowledges the Secretaría de Ciencia, Humanidades, Tecnología e Innovación for the doctoral scholarship, CVU No. 244745. The authors would like to acknowledge the support provided by Roberto Hernández Reyes, Samuel Tehuacanero Cuapa, Juan Gabriel Morales Morales, Carlos Magaña, Carolina Bohórquez Martínez, Diego Quiterio and José Ángel Flores Orozco for technical assistance in TEM, SEM, and sample preparation, respectively. All funding for the realization and publication of this research work came from the following projects: (a) PAPIIT-UNAM project number: IN111723; and (c) CONACYT-Apoyos para Adquisición y Mantenimiento de Infraestructura en Instituciones y Laboratorios de Investigación Especializada 2019, project number: 299881, which are under the technical administration of Arturo Rodríguez-Gómez. Arturo Rodríguez-Gómez wishes to express his profound gratitude to God Almighty.

Conflict of interest

The author(s) declared that this work was conducted in the absence of any commercial or financial relationships that could be construed as a potential conflict of interest.

Generative AI statement

The author(s) declared that generative AI was used in the creation of this manuscript. Generative AI was used exclusively for language editing, grammar correction, and improvements in writing style. No scientific content, data analysis, or interpretation was generated by AI; its use was strictly limited to the refinement of the manuscript's written expression.

Any alternative text (alt text) provided alongside figures in this article has been generated by Frontiers with the support of artificial intelligence and reasonable efforts have been made to ensure accuracy, including review by the authors wherever possible. If you identify any issues, please contact us.

Publisher's note

References

1. Le-Nian He L-NH, Takao Inokuma TI, Seiichi Hasegawa SH. Properties of "Stoichiometric" silicon oxynitride films. *Jpn J Appl Phys* (1996) 35:1503. doi:10.1143/JJAP.35.1503

2. Xiang C, Jin W, Bowers JE. Silicon nitride passive and active photonic integrated circuits: trends and prospects. *Photon Res* (2022) 10:A82. doi:10.1364/PRJ.452936

3. Shi Y, He L, Guang F, Li L, Xin Z, Liu R. A review: preparation, performance, and applications of silicon oxynitride film. *Micromachines* (2019) 10:552. doi:10.3390/mi10080552

4. Trinh TT, Jang K, Nguyen VD, Dao VA, Yi J. Role of SiOxNy surface passivation layer on stability improvement and kink effect reduction of ELA poly silicon thin film transistors. *Microelectron Eng* (2016) 164:14–9. doi:10.1016/j.mee.2016.07.002

5. Won LJ, Kyu Jin C, Yong Lim K, Jae Lee Y, Kim S-R, Choi B-I, et al. Transparent high-performance SiOxNy/SiOx barrier films for organic photovoltaic cells with high durability. *Nano Energy* (2017) 33:12–20. doi:10.1016/j.nanoen.2017.01.022

6. Park J-H, Shin M-H, Yi J-S. The characteristics of transparent non-volatile memory devices employing Si-Rich SiOX as a charge trapping layer and indium-tin-zinc-oxide. *Nanomaterials* (2019) 9:784. doi:10.3390/nano9050784

7. Wo¨rhoff K, Hilderink LTH, Driessen A, Lambeck PV. Silicon oxynitride. *J Electrochem Soc* (2002) 149:F85. doi:10.1149/1.1486240

8. Barrera-Mendivelso ES, Rodríguez-Gómez A. Thin films of silicon nitride deposited at room temperature by non-reactive magnetron sputtering: radiofrequency power and deposition time influence on the formation of α-Si3N4 and its optical properties. *Front Phys* (2023) 11:1–13. doi:10.3389/fphy.2023.1260579

9. Ortiz-Santos A, Ramos C, Sastré-Hernández J, Santana G, Dutt A. White electroluminescence from SiN x thin films by a PECVD equipment using dichlorosilane precursor and study of emission mechanism. *Mater Technol* (2019) 1–8. doi:10.1080/10667857.2019.1603185

10. de Ridder RM, Warhoff K, Driessen A, Lambeck PV, Albers H. Silicon oxynitride planar waveguiding structures for application in optical communication. *IEEE J Sel Top Quan Electron* (1998) 4:930–7. doi:10.1109/2944.736079

11. Germann R, Salemink HWM, Beyeler R, Bona GL, Horst F, Massarek I, et al. Silicon oxynitride layers for optical waveguide applications. *J Electrochem Soc* (2000) 147:2237. doi:10.1149/1.1393513

12. Wang J, Bouchard JP, Hart GA, Oudard JF, Paulson CA, Sachenik PA, et al. Silicon oxynitride based scratch resistant anti-reflective coatings. In: BF Andresen, PL Marasco, JS Sanghera, MP Snyder, JN Vizgaitis, editors. *Advanced optics for defense applications: UV through LWIR III*, 15. SPIE (2008). 15. doi:10.1117/12.2303679

13. Piccoli G, Sanna M, Borghi M, Pavesi L, Ghulinyan M. Silicon oxynitride platform for linear and nonlinear photonics at NIR wavelengths. *Opt Mater Express* (2022) 12:3551. doi:10.1364/OME.463940

14. Chin M-K, Lee C-W, Lee S-Y, Darmawan S. High-index-contrast waveguides and devices. *Appl Opt* (2005) 44:3077–86. doi:10.1364/AO.44.003077

15. Ning T, Pietarinen H, Hyvärinen O, Simonen J, Genty G, Kauranen M. Strong second-harmonic generation in silicon nitride films. *Appl Phys Lett* (2012) 100:161902. doi:10.1063/1.4704159

16. Xu Y-N, Ching WY. Electronic structure and optical properties of α and β phases of silicon nitride, silicon oxynitride, and with comparison to silicon dioxide. *Phys Rev B* (1995) 51:17379–89. doi:10.1103/PhysRevB.51.17379

17. Blumenthal DJ, Heideman R, Geuzebroek D, Leinse A, Roeloffzen C. Silicon nitride in silicon photonics. *Proc IEEE* (2018) 106:2209–31. doi:10.1109/JPROC.2018.2861576

18. Wong CK, Wong H, Kok CW, Chan M. Silicon oxynitride prepared by chemical vapor deposition as optical waveguide materials. *J Cryst Growth* (2006) 288:171–5. doi:10.1016/j.jcrysgro.2005.12.022

19. Kuiper AET, Koo SW, Habraken FHPM, Tamminga Y. Deposition and composition of silicon oxynitride films. *J Vac Sci Technol B Microelectron Process Phenom* (1983) 1:62–6. doi:10.1116/1.582543

20. Beck RB, Giedz M, Wojtkiewicz A, Kudła A, Jakubowski A. PECVD formation of ultrathin silicon nitride layers for CMOS technology. *Vacuum* (2003) 70:323–9. doi:10.1016/S0042-207X(02)00665-6

21. Santana G, Morales-Acevedo A. Optimization of PECVD SiN:H films for silicon solar cells. *Sol Energy Mater Sol Cells* (2000) 60:135–42. doi:10.1016/S0927-0248(99)00078-1

22. Rodriguez-Gómez A, García-Valenzuela A, Haro-Poniatowski E, Alonso-Huitrón JC. Effect of thickness on the photoluminescence of silicon quantum dots embedded in silicon nitride films. *J Appl Phys* (2013) 113:233102. doi:10.1063/1.4811361

23. Muñoz-Rosas A, Rodríguez-Gómez A, Alonso-Huitrón J. Enhanced electroluminescence from silicon quantum dots embedded in silicon nitride thin films coupled with gold nanoparticles in light emitting devices. *Nanomaterials* (2018) 8:182. doi:10.3390/nano8040182

24. Rodríguez-Gómez A, Moreno-Rios M, García-García R, Pérez-Martínez AL, Reyes-Gasga J. Role of the substrate on the growth of silicon quantum dots embedded in silicon nitride thin films. *Mater Chem Phys* (2018) 208:61–7. doi:10.1016/j.matchemphys.2018.01.032

25. Muñoz-Rosas AL, Rodríguez-Gómez A, Arenas-Alatorre JA, Alonso-Huitrón JC. Photoluminescence enhancement from silicon quantum dots located in the vicinity of a monolayer of gold nanoparticles. *RSC Adv* (2015) 5:92923–31. doi:10.1039/C5RA19114A

26. Rodríguez-Gómez A, Escobar-Alarcón L, Serna R, Cabello F, Haro-Poniatowski E, García-Valenzuela A, et al. Modeling of the refractive index and composition of luminescent nanometric chlorinated-silicon nitride films with embedded Si-quantum dots. *J Appl Phys* (2016) 120:145305. doi:10.1063/1.4964812

27. Rodríguez A, Arenas J, Pérez-Martínez AL, Alonso JC. Role of ammonia in depositing silicon nanoparticles by remote plasma enhanced chemical vapor deposition. *Mater Lett* (2014) 125:44–7. doi:10.1016/j.matlet.2014.03.144

28. Sazonov A, Nathan A, Striakhilev D. Materials optimization for thin film transistors fabricated at low temperature on plastic substrate. *J Non Cryst Sol* (2000) 266:1329–34. doi:10.1016/s0022-3093(99)00946-1

29. Hegedüs N, Lovics R, Serényi M, Zolnai Z, Petrik P, Mihály J, et al. Examination of the hydrogen incorporation into radio frequency-sputtered hydrogenated SiNx thin films. *Coatings* (2021) 11:1–13. doi:10.3390/coatings11010054

30. Aissani L, Alhussein A, Zia AW, Mamba G, Rtimi S. Magnetron sputtering of transition metal nitride thin films for environmental remediation. *Coatings* (2022) 12:1–29. doi:10.3390/coatings12111746

31. Yeboah LA, Oppong PA, Malik AA, Acheampong PS, Morgan JA, Addo RAA, et al. Exploring innovations, sustainability and future opportunities in semiconductor technologies. *Int J Adv Nano Comput Anal* (2024) 3:3. doi:10.61797/ijanca.v3i2.348

32. Aborah YL, Agyemang Oppong P, Abdul Malik A, Sarfo Acheampong P, Arko Morgan J, Akua Adwubi Addo R, et al. Sustainable manufacturing and applications of wide-bandgap semiconductors—A review. *Intell Sustain Manuf* (2025) 2:10010. doi:10.70322/ism.2025.10010

33. Dergez D, Schneider M, Bittner A, Pawlak N, Schmid U. Mechanical and electrical properties of RF magnetron sputter deposited amorphous silicon-rich silicon nitride thin films. *Thin Solid Films* (2016) 606:7–12. doi:10.1016/j.tsf.2016.03.029

34. Mirsch S, Bauer J. Properties of silicon nitride and silicon oxynitride films prepared by reactive sputtering. *Phys Status Solidi* (1974) 26:579–84. doi:10.1002/pssa.2210260222

35. Rodríguez-López R, Soto-Valle G, Sanginés R, Abundiz-Cisneros N, Águila-Muñoz J, Cruz J, et al. Study of deposition parameters of reactive-sputtered Si3N4 thin films by optical emission spectroscopy. *Thin Solid Films* (2022) 754:139313. doi:10.1016/j.tsf.2022.139313

36. Wang Y, Qu H, Wang Y, Dong F, Chen Z, Zheng W. Radio frequency plasma-enhanced reactive magnetron sputtering deposition of α-sinx on photonic crystal-laser diodes for facet passivation. *ACS Omega* (2019) 4:20205–11. doi:10.1021/acsomega.9b02452

37. Mustafa MK, Majeed U, Iqbal Y. Effect on silicon nitride thin films properties at various powers of RF magnetron sputtering. *Int J Eng Technol* (2018) 7:39–41. doi:10.14419/ijet.v7i4.30.22000

38. De Luca D, Di Gennaro E, De Maio D, D'Alessandro C, Caldarelli A, Musto M, et al. Tuning silicon nitride refractive index through radio-frequency sputtering power. *Thin Solid Films* (2021) 737:737. doi:10.1016/j.tsf.2021.138951

39. Chen W-J, Liu Y-C, Wang Z-Y, Gu L, Shen Y, Ma H-P. Physical and electrical properties of silicon nitride thin films with different nitrogen–oxygen ratios. *Nanomaterials* (2025) 15:958. doi:10.3390/nano15130958

40. Cisneros-Contreras IR, López-Ganem G, Sánchez-Dena O, Wong YH, Pérez-Martínez AL, Rodríguez-Gómez A. Al-Doped ZnO thin films with 80% average transmittance and 32 ohms per square sheet resistance: a genuine alternative to commercial high-performance indium tin oxide. *Physics (College Park Md)* (2023) 5(5):45–58. doi:10.3390/physics5010004

41. Godyak VA, Piejak RB, Alexandrovich BM. Electron energy distribution function measurements and plasma parameters in inductively coupled argon plasma. *Plasma Sourc Sci Technol* (2002) 11:525–43. doi:10.1088/0963-0252/11/4/320

42. Kramida A, Ralchenko Y, Reader J. NIST atomic spectra database. (2023) doi:10.18434/T4W30F

43. Garrido-García LF, Pérez-Martínez AL, Reyes-Gasga J, Aguilar-Del-Valle Mdel P, Wong YH, Rodríguez-Gómez A. A simple methodology to gain insights into the physical and compositional features of ternary and Quaternary compounds based on the weight percentages of their constituent elements: a proof of principle using conventional EDX characterizations. *Ceramics* (2024) 7:1275–300. doi:10.3390/ceramics7030085

44. Wyckoff RWG. *Crystal structures*. 2nd edition. New York: Interscience Publishers (1963). Available online at: https://worldcat.org/title/473923608 (Accessed 16 August 2024).

45. Yang P, Fun H-K, Rahman IA, Saleh MI. Two phase refinements of the structures of α-Si3N4 and β-Si3N4 made from rice husk by rietveld analysis. *Ceram Int* (1995) 21:137–42. doi:10.1016/0272-8842(95)95885-L

46. Zhang P, Zhang L, Ge X, Wang S. Tunable luminescent A-SiNxOy films with high internal quantum efficiency and fast radiative recombination rates. *Materials (Basel)* (2018) 11:2494. doi:10.3390/ma11122494

47. Rai H, Singh KRB, Pandey SS, Natarajan A. Role of Si and SiO_2 in optoelectronic device fabrication. *J Mol Struct* (2024) 1316:138994. doi:10.1016/j.molstruc.2024.138994

48. Rai H, Singh KRB, Natarajan A, Pandey SS. Advances in field effect transistor based electronic devices integrated with CMOS technology for biosensing. *Talanta Open* (2025) 11:100394. doi:10.1016/j.talo.2024.100394